Aerosol optical properties within the atmospheric boundary layer predicted from ground-based observations compared to Raman lidar retrievals during RITA-2021

Xinya Liu[1], Diego Alves Gouveia[2], Bas Henzing[3], Arnoud Apituley[2], Arjan Hensen[3], Danielle van Dinther[3], Rujin Huang[4], Ulrike Dusek[1]

[1]Centre for Isotope Research (CIO), Energy and Sustainability Research Institute Groningen (ESRIG), University of Groningen, Groningen, 9747 AG, the Netherlands
[2]Royal Netherlands Meteorological Institute (KNMI), De Bilt, 3730 AE, the Netherlands
[3]Department of Climate, Air and Sustainability, TNO, Utrecht, 3584 CB, the Netherlands
[4]State Key Laboratory of Loess and Quaternary Geology, Center for Excellence in Quaternary Science and Global Change, and Key Laboratory of Aerosol Chemistry and Physics, Institute of Earth and Environment, Chinese Academy of Sciences, Xi'an 710061, China

Correspondence to: Ulrike Dusek (u.dusek@rug.nl)

Abstract

In this study, ~~a Mie theory based model was built to predict the vertical profile of the~~we utilized ground-based in-situ measurements of the aerosol chemical composition and particle size distribution, as well as meteorological data from the Weather Forecasts (ECMWF) to predict vertical profiles of aerosol optical properties, including the aerosol scattering coefficient, backscatter coefficient, extinction coefficient, and lidar ratio. ~~The model utilizes ground based in situ measurements of the aerosol chemical composition and particle size distribution, as well as the meteorological data from the Weather Forecasts (ECMWF) as input values. These are all parameters readily obtained for ACTRIS sites and the aim of this study was to investigate their suitability for generating representative estimates of the lidar ratio, and then further improve the lidar retrievals by utilizing these estimates. The measurements were performed during the Ruisdael land atmosphere interactions Intensive Trace gas and Aerosol (RITA) campaign in the Netherlands in 2021. The calculated dry aerosol optical properties were validated against a Nephelometer with good agreements ($R^2 \approx 0.9$).~~ The predicted ambient ~~vertical~~ profiles ~~of aerosol optical properties~~ were compared to retrievals by a multi-wavelength Raman lidar~~.~~ during the Ruisdael Intensive Trace-gas and Aerosol (RITA) campaign in the Netherlands in 2021 for 26 time periods of approximately 1 hour each. Predicted and retrieved extensive aerosol properties (scattering, backscatter ~~coefficients~~and extinction coefficient) were ~~usually~~comparable only approximately 35% of the time, mostly under ~~conditions~~the condition of ~~a~~ well-mixed boundary ~~layer. The extinction coefficients and lidar ratios were~~layers. In this case, ground-based measurements can provide a way to extend extinction profiles to lower altitudes, where they cannot be retrieved ~~by~~, as well as to verify the ~~Raman~~ lidar ~~only at a height above 800 m. The estimated~~measured profiles. On the other hand, the lidar ratio profiles predicted by ground-based ~~on in situ~~ data ~~connected~~compared reasonably well to the ~~lidar profiles within the boundary layer, with differences on average~~retrieved lidar profiles (starting at 800 m) also for conditions where the predicted and retrieved backscatter profiles differed considerably. The difference in predicted and retrieved lidar ratio is usually less than $\pm$ 30%. Our study thus shows that for well-mixed

boundary layers, a representative lidar ratio can be estimated based on ground-based in-situ measurements of dry size distribution and chemical composition taking into account the hygroscopic growth and ambient humidity. ~~This allows to extend extinction profiles to lower altitudes, where they cannot be retrieved, or for use with simple elastic backscatter lidar to derive extinction profiles. The proposed method could be further applied to predict aerosol optical depth and also might be beneficial for large scale or global radiation simulations~~This approach offers a method of providing lidar ratios calculated from independent in-situ measurements for simple backscatter lidars or at times, when Raman lidar profiles cannot be measured (e.g. during the day-time). It uses only data that are routinely available at aerosol measurement stations and is therefore not only useful for further validating lidar measurements but also for bridging the gap between in situ measurements and lidar remote sensing.

1   Introduction

Aerosols play an important role in climate change by altering the earth's radiation budget through their interaction with solar radiation. Aerosols reflect part of the sunlight, thereby reducing the radiation at the earth's surface (Twomey, 1977; IPCC, 2013), which results in a cooling effect. On the other hand, certain types of aerosols can also absorb solar radiation, which locally warms the atmosphere and results in a change of the temperature profile, further affecting the atmospheric circulations ~~(Koren et al., 2008; Rosenfeld et al., 2014; Bréon, 2006).~~(Koren et al., 2008; Rosenfeld et al., 2014; Bréon, 2006). In addition, aerosol particles can act as cloud condensation nuclei or ice nuclei affecting the microphysical properties of clouds, and thereby affect the radiation budget indirectly ~~(Graf, 2004; Lohmann and Feichter, 2005; Bréon, 2006).~~(Graf, 2004; Lohmann and Feichter, 2005; Bréon, 2006). There are still large uncertainties in predicting the contribution of aerosol radiative forcing to climate change, due to the complexity of microphysical and chemical process and their dynamic feedback on the aerosol budget ~~(Kaufman et al., 2005; Feingold, 2001; Graf, 2004)~~(Kaufman et al., 2005; Feingold, 2001; Graf, 2004). To reduce the uncertainties, observation and simulation of aerosol optical properties and their vertical profiles are essential for a better understanding of aerosol radiative forcing (Moise et al., 2015; Chang et al., 2006).

~~Light detection and ranging (lidar) is a widely used active remote sensing method for studying the spatial distribution aerosol optical properties (Sicard et al., 2011; Kim et al., 2007; Bhardwaj et al., 2016; Markowicz et al., 2016).~~Light detection and ranging (lidar) is a widely used active remote sensing method for studying the spatial distribution aerosol optical properties (Collis and Russell, 1976; Measures, 1984; Whiteman et al., 1992; Weitkamp, 2005). The detected signal of the elastically backscattered light can be converted into the backscatter and extinction coefficients based on an analytical solution of the so-called "lidar equation" (Klett, 1981; Fernald, 1984) with the assumption of a given extinction to backscatter ratio, called the "lidar ratio". However, the lidar ratio is governed by many factors such as the wavelength of incoming light, the aerosol chemical composition, particle size distribution, relative humidity, and other atmospheric conditions ~~(Noh et al., 2008; Balis et al., 2004; Lopes et al., 2013; Shin et al., 2018; Dawson et al., 2015; Moise et al., 2015).~~(Salemink et al., 1984; Floutsi et al., 2023). Large errors can occur when retrieving aerosol extinction from backscattered signals. Thus, a Raman lidar technique based on Raman spectroscopy was developed to address this problem (Ansmann et al., 1990). ~~The profiles of the backscatter~~

~~and the extinction coefficient can be determined independently by the Raman lidar, without the assumption of a lidar ratio (Cooney et al., 1969; Melfi, 1972; Ansmann et al., 1990, 1992).~~ The profiles of the backscatter and the extinction coefficient can be determined independently by the Raman lidar, without the assumption of a lidar ratio (Ansmann et al., 1992a, b). However, a common limitation on the accuracy of the lidar-based retrievals emerges for distances close to the instrument where only a fraction of the atmospheric volume illuminated by the laser pulse is within the lidar's receiver field-of-view, resulting in a "blind zone" at the instrument (no overlap) and a region that is gradually becoming visible for the receiver after some distance (incomplete overlap region) ~~(Wandinger, 2005). While Raman backscatter retrials can be~~ (Wandinger and Ansmann, 2002). While Raman backscatter retrials are less affected by the incomplete overlap region, Raman extinction and elastic lidar retrievals are particularly sensitive to it, even after an overlap correction is applied, and thus it can only accurately record the aerosol profiles above a certain altitude ~~(Rosati et al., 2016; Hervo et al., 2016; Wandinger and Ansmann, 2002)~~ (Hervo et al., 2016; Wandinger and Ansmann, 2002).

Besides active remote sensing, vertical aerosol profiles can also be measured by in situ airborne instruments (Düsing et al., 2021; Haarig et al., 2019; Düsing et al., 2018). These give more accurate information, but are expensive and time consuming and thus lack the temporal coverage of lidar measurements. They are essential in the evaluation of the lidar retrievals and several studies have modelled the aerosol optical vertical profiles based on the Mie theory using the vertically resolved aerosol information but measured by the airborne instruments (Düsing et al., 2021; Ferrero et al., 2019; Düsing et al., 2018). Their results support the usefulness of in situ observations for evaluation of lidar retrievals, however, there are only a few profiles available due to the high cost of the airborne measurements.

In this study, we evaluate a method to predict vertical profiles of the aerosol optical properties using ground-based in situ measurements of the aerosol chemical composition and particle size distribution combined with meteorological profiles from the European Centre for Medium-Range Weather Forecasts (ECMWF). The experiments were performed at Cabauw Experimental Site for Atmospheric Research (CESAR) site in the Netherlands during the Ruisdael land-atmosphere interactions Intensive Trace-gas and Aerosol (RITA) 2021 field campaign[1]. The primary goal of this study is to evaluate if routine ground-based measurements can be used to predict the lidar ratio and the extinction coefficient in the lower atmosphere, where it cannot be retrieved by the Raman lidar. If successful, this information can then be used to extrapolate extinction profiles to the ground or to derive extinction data from elastic backscatter lidars. A further goal is to explore under which circumstances the aerosol measured on the ground can represent the vertical aerosol distribution in the atmosphere. The advantage of the proposed method is that we use only ground-based data that are readily available at most lidar sites and the easily obtained ECMWF data.

---

[1] https://ruisdael-observatory.nl/the-rita-2021-campaign/

2   Methods

2.1   Experiment site and campaign description

The RITA campaign was carried out at the CESAR in the Netherlands (51.97∘ N, 4.93∘ E) during Spring (11th May - 24th May)
and during Fall (16th September - 12th October) in 2021. CESAR is one of the core observatories for the Ruisdael[2] observatory
and also part of the ACTRIS[3] (Aerosol, Clouds and Trace Gases Infra-Structure) and ICOS[4] (Integrated Carbon Observation
System). An aerial view of the infrastructure setup during the RITA campaign and the CESAR location are shown in Figure
S11. The site is situated in a polder 0.7 m below average sea level and surrounded by a flat pasture landscape. The mode of
the wind direction distributions was southwest, but winds were also coming from the northeast as shown in Figure S2, so the
potential pollution sources could be from Rotterdam with its large international harbour but also from nearby Utrecht. The
ground-based aerosol in situ measurements included the aerosol chemical composition, particle size distribution and aerosol
optical properties. Two intensive measurement campaigns were performed during Spring (11th May - 24th May) and during Fall
(16th September - 12th October). The remote sensing observations by the Raman lidar were obtained regularly during the
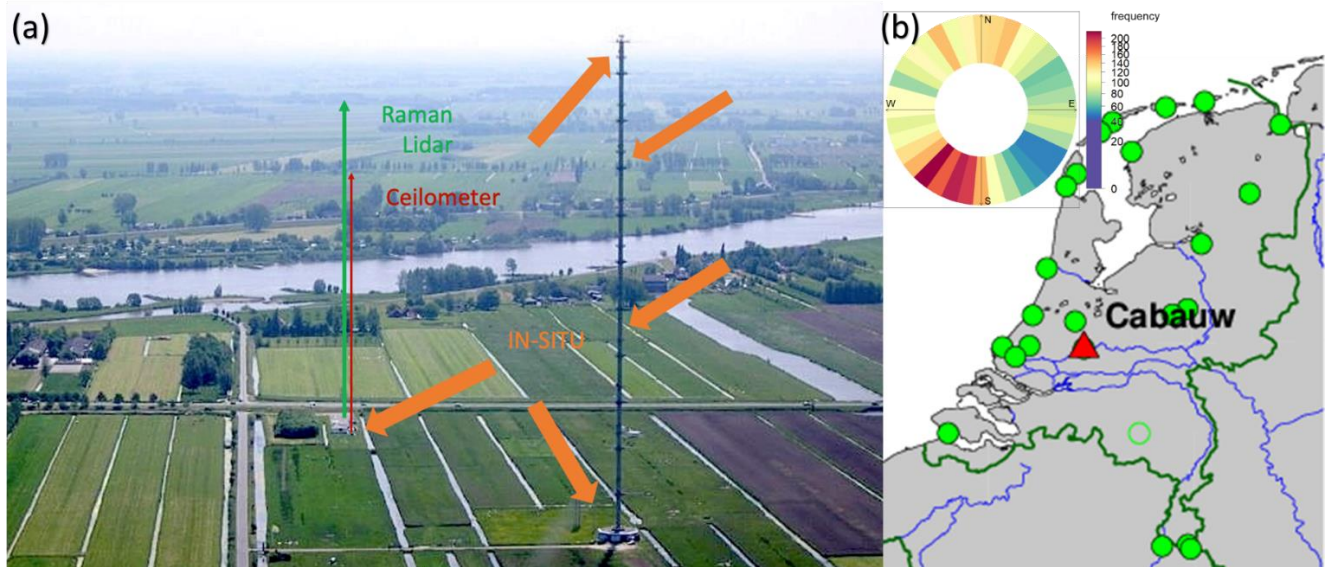campaign depending on the atmospheric conditions.

Figure 1: (a) An aerial view of the infrastructure setup during the RITA-2021campaign (photo by Wouter Knap, KNMI). (b) The frequency of the hourly average wind direction at CESAR in RITA campaign from May 7th 2021 to October 20th 2021 and the site (marked in red) location in the Netherlands[5].

---

[2] https://ruisdael-observatory.nl/ (last access: 20 July 2022)
[3] http://actris.net/ (last access: 20 July 2022)
[4] https://www.icos-cp.eu/ (last access: 20 July 2022)
[5] http://gnss1.tudelft.nl/dpga/station/Cabauw.html

2.1.1 Aerosol chemical composition measurements

115 Aerosol chemical composition was measured by different online and offline methods during the campaign.

(i) A time of flight-aerosol chemical species monitor (TOF-ACSM; Aerodyne Research Inc., Billerica, MA) equipped with capture vaporizer (CV) and $PM_{2.5}$ lens measured the mass concentration of non-refractory chemical compounds with a 10-minute time resolution. The TOF-ACSM was installed in a trailer, which was next to the remote sensing site as shown in the Figure ~~S1~~1(a) approximately 200 m distant from the other in situ measurements. The inlet was a Teflon Coated Aluminum

120 cyclone (URG 2000-30ED) with an aerodynamic cut-off diameter of 2.5 µm at ambient conditions and the inlet flow rate was 2.3 L min^{-1} controlled by the ARI Sample Line Flow Controller (S/N FCB-023) at the head of the TOF-ACSM inlet. Particles were dried by a Nafion dryer (Perma Pure, New Jersey). Five chemical species, namely ammonium (NH_4^+), nitrate (NO_3^-), sulphate (SO_4^{2-}), chloride (Cl^-), and organics (Org), were derived based on the fragmentation tables for TOF-ACSM (Fröhlich et al., 2013). The standard calibrations, such as the flow rate calibration, lens calibration and heater bias (HB) voltage tuning

125 were performed before and after the campaign. Ionization efficiency (IE) and the relative ionization efficiency (RIE) were determined by calibration with NH_4NO_3 and $(NH_4)_2SO_4$ solutions with a concentration of 0.005 Mol L^{-1}. The calibration values used in this study are: IE NO_3 = 258.20 pg s^{-1}; RIE NH_4 = 3.51; RIE SO_4 = 1.33; RIE Org =1.40; RIE Chl=1.30; at an air beam (AB) = 4.55E + 5 ions s^{-1}; flow rate = 1.46 cm^3 s^{-1}. The data were processed by the Tofware software (version of 3.2.4, Tofwerk AG, Thun, Switzerland).

130 **(ii)** $PM_{2.5}$ and PM_{10} filter samples were collected for 24 hours using a SEQ47/50 (Leckel GmbH, Germany) instrument with a sequential low-volume system (LVS) of 2.3 m^3 h^{-1} next to the trailer with the TOF-ACSM. The sampler operation was based on the European Standards (EN12341: 1998 and EN14907: 2005). The filter samples were collected under ambient conditions, stored at approximately -20°C, and protected using ice packs during transportation. The concentrations of 3 inorganic anions (NO_3^-, Cl^-, SO_4^{2-}) and 5 cations (Na^+, K^+, Mg_2^+, Ca_2^+, NH_4^+) were determined by chromatography (ICS-1100, Thermo

135 Scientific). Organic carbon (OC) and elemental carbon (EC) were analysed by a Sunset thermal optical analyzer (TOA, Sunset Laboratory Inc.) using the EUSAAR2 protocol (F. Cavalli, M. Viana, K. E. Yttri, J. Genberg, 2010; Karanasiou et al., 2020). The details of the data evaluation can be found in Liu et al., (~~2023~~2023b).

~~(iii) the equivalent Black Carbon (eBC) mass concentration was measured by the multi-angle absorption photometer (MAAP model 5012, Thermo Fisher Scientific Inc., Franklin, MA) with 5-minute time resolution (Petzold and Schönlinner, 2004;~~

140 ~~Petzold et al., 2005). A constant scattering cross section value (6.6 m²g⁻¹) based on the user handbook was given for converting the aerosol light absorption coefficient at 670 nm.~~

~~The MAAP and the other in situ measurements discussed below were installed in the Cabauw main building, underneath the 213 m high tower as displayed in Figure S1.~~**(iii)** the equivalent Black Carbon (eBC) mass concentration was measured by the multi-angle absorption photometer (MAAP model 5012, Thermo Fisher Scientific Inc., Franklin, MA) with 5 minute time

145 resolution (Petzold and Schönlinner, 2004; Petzold et al., 2005). A constant scattering cross section value (6.6 m^2 g^{-1}) based on the user handbook was given for converting the aerosol light absorption coefficient at 670 nm.

The MAAP and the other in situ measurements discussed below were installed in the Cabauw main building, underneath the 213 m high tower as displayed in Figure 1. The MAAP was measuring behind a PM$_{10}$ inlet that was situated 4.5 m above the ground on the roof. A wide diameter Nafion drying system were installed after the PM$_{10}$ size selector to dry the ambient aerosol to an RH below 40%. After the Nafion a manifold split the aerosol flow equally to the multiple instruments. An overview of the chemical composition and meteorological information of the in situ measurements from the May to November in 2021 is displayed in the Figure S3.

2.1.2   Particle size distribution measurements

The particle number size distribution (PNSD) was measured by a Scanning Mobility Particle Size Spectrometer (MPSS, TROPOS) and an Aerodynamic particle sizer spectrometer (APS, Model 3321, TSI) which were connected to the same inlet as the MAAP. The MPSS measures particles in the size range from ~10 to 800 nm in electromobility diameter with a time resolution of 5 minutes. Before entering the MPSS, the particles are dried to below 40% relative humidity (RH) by a Perma Pure Nafion air dryer and then charged by a bipolar particle charger (Ni-63). The recorded data was inverted by a custom evaluation software (DMPS-Inversion-2.13.exe) correcting for the diffusion losses of the particles, bipolar charge equilibrium, and the DMA transfer function, as well as the CPC counting efficiency (Wiedensohler et al., 2012). The APS (Peters and Leith, 2003) covers an aerodynamic size range from 0.5 to 20 µm with data recorded in 1-minute time resolution. However, due to the inlet size cut off, the valid size range of the APS is from 0.5 to 10 µm.

The MPSS and APS measured size distributions were merged to create a particle size distribution with a diameter range from 10 nm to 10 µm following the method of Modini et al.(2021). We used the hourly merged particle size distribution to calculate the optical properties for a 5-month period and then compared with the nephelometer measurement. To calculate the vertical profiles, the PNSD data is averaged at a time resolution of 10 minutes. Subsequently, the nearest time period within the radar measurement range is selected for averaging. In this study, the MPSS electrical mobility diameters were assumed to correspond to volume-equivalent diameter, then APS aerodynamic diameters were converted to volume equivalent diameters. However, shape effects were neglected. The details of joining the PNSD are described in the supplementary material in section S2 as shown and an example is given in Figure S4S1.

2.1.3   Ground-based measurements of aerosol optical properties

The aerosol scattering and backscatter coefficient were measured with a 5-minute time resolution by a three-wavelength integrating nephelometer (Dry Neph, TSI Inc., Model 3563) located in the main building adjacent to the MAAP. The Nephelometer measured the aerosol scattering coefficient using a wide angular integration (from 7 to 170°) and the backscatter integrated from 90 to 170° (Anderson et al., 1996; Anderson and Ogren, 1998; Heintzenberg and Charlson, 1996). Scattering coefficients integrated from 0 to 180° were derived based on the truncation correction function proposed in Anderson and Ogren (1998). The truncation error ranges from approximately 5% to 10% for submicron particles and from 30% to 50% for particles between 1 and 10µm (Anderson and Ogren, 1998; Anderson et al., 1996; Muller et al., 2009).

6

The three-wavelength integrating nephelometer (Dry Neph, TSI Inc., Model 3563) was used to measure the surface aerosol scattering coefficient in a wide angular integration (from 7 to 170°) and the backscatter coefficient (from 90 to 170°) (Anderson et al., 1996; Anderson and Ogren, 1998; Heintzenberg and Charlson, 1996). Scattering coefficients integrated from 0 to 180° were derived based on the truncation correction function proposed in Anderson and Ogren (Anderson and Ogren, 1998). The truncation error ranges from approximately 5% to 10% for submicron particles and from 30% to 50% for particles between 1 and 10µm (Anderson and Ogren, 1998; Anderson et al., 1996; Muller et al., 2009). The instrument was located in the main building adjacent to the MAAP and data was collected with a 5-minute time resolution.

2.2 Meteorological observations

The meteorological data used in this study are obtained from the ACTRIS data portal[6], which are the Near Real Time (NRT) data generated by the ECMWF IFS forecast Model with 1-hour time resolution. ~~Figure S5 shows the~~The RH and temperature profiles derived from the ECMWF model ~~from May to November~~was used in ~~2021~~this study. In situ measured meteorological parameters at different heights (7 m, 10 m, 20 m, 40 m, 80 m, 140 m, 200 m) were also recorded cat the 213 m high mast of CESAR tower with a 10-minute time resolution. Data available from May to June in 2021 and can be requested from the KNMI Data Platform[7]. However, we need meteorological profiles that cover the boundary layer depth reaching far beyond the tower height. A radiometer (RPG-HATPRO) located at the CESAR remote sensing site provided vertical profiles of RH and temperature from May to October in 2021. In addition, in-situ measurements of meteorological data were provided by a radiosonde (Vaisala RS92-SGP) carried on a balloon, which was launched every day at around 00:00 UTC from the De Bilt, approximately 25 km from the CESAR site. Previous studies (Fernández et al., 2015; Apituley et al., 2009) concluded that the atmospheric conditions at the CESAR observatory and at the De Bilt site are not significantly different. Therefore, the in-situ measurements from radiosonde were used to evaluate the meteorological profiles during the campaign period ~~(in Figure S6).~~. The findings demonstrated that the ECMWF data closely align with the in-situ measurements from the radiosonde by the balloon. Consequently, the ECWMF data was chosen and subsequently utilized in the calculations.

2.3 Remote sensing measurements

2.3.1 CAELI Raman lidar

CAELI is a high power multiwavelength Raman lidar system that is specifically designed for profiling water vapor, aerosols, and clouds (Apituley et al., 2009). CAELI uses a pulsed neodymium-doped yttrium aluminium garnet (Nd:YAG) laser as the light source, emitting laser pulses at 1064 nm (IR), 532 nm (VIS), and 355 nm (UV). The laser and receiver are aligned in a dual-axis configuration with a single target axis pointing vertically to the zenith. The receiving system uses Newtonian telescopes and separate optical channels, with three elastic channels (1064, 532, and 355 nm) and three Raman channels (387

---

[6] https://cloudnet.fmi.fi/ (last access 20 July 2022)
[7] https://dataplatform.knmi.nl(last access: 20 July 2022)

and 607 nm (nitrogen) and 407 nm (water vapor)) to detect the backscattered light signals in the atmosphere. For full tropospheric coverage, CAELI's receiving system is duplicated using a 15 and a 57 cm telescopes for near field range (NFR) and far field range (FFR) measurements respectively. More details on CAELI can be found in Apituley et al. (2009). For this study, the lidar aerosol optical products were retrieved using the EARLINET Single Calculus Chain (SCC) using CAELI's near field telescope measurements and atmospheric model data (D'Amico et al., 2015). To increase signal-to-noise ratio, the raw data vertical resolution was reduced to 60 m and the profiles were usually accumulated for about 1 hour. The Raman backscatter profiles are available starting from 150 m above ground, while the elastic backscatter and Raman extinction coefficient were retrieved above 810 m. To avoid the effects of an incomplete overlap on the extinction retrievals, a post-processing step consisted in removing the extinction profile below the full overlap height (690 m for a telecover test deviation < 3%) plus the effective vertical resolution of the extinction retrieval (Mattis et al., 2016), which resulted in a minimum usable Raman extinction profile typically above 810-1050 m depending on the aerosol load, solar background, and fraction of cloud screened profiles. (overlap function over 97%). To account for the remaining effects of the incomplete overlap above this altitude on the extinction retrievals, an overlap correction was applied based on the method proposed by Wandinger and Ansmann (2002).
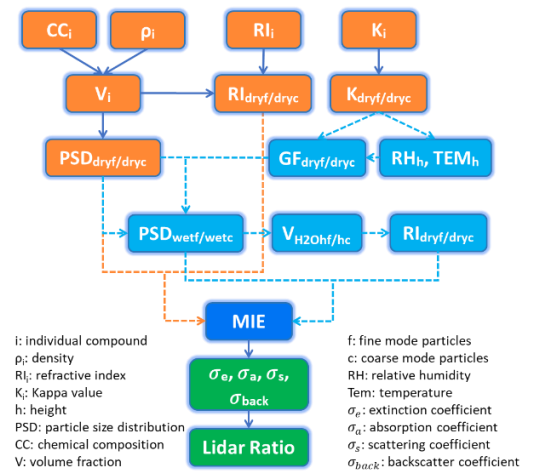
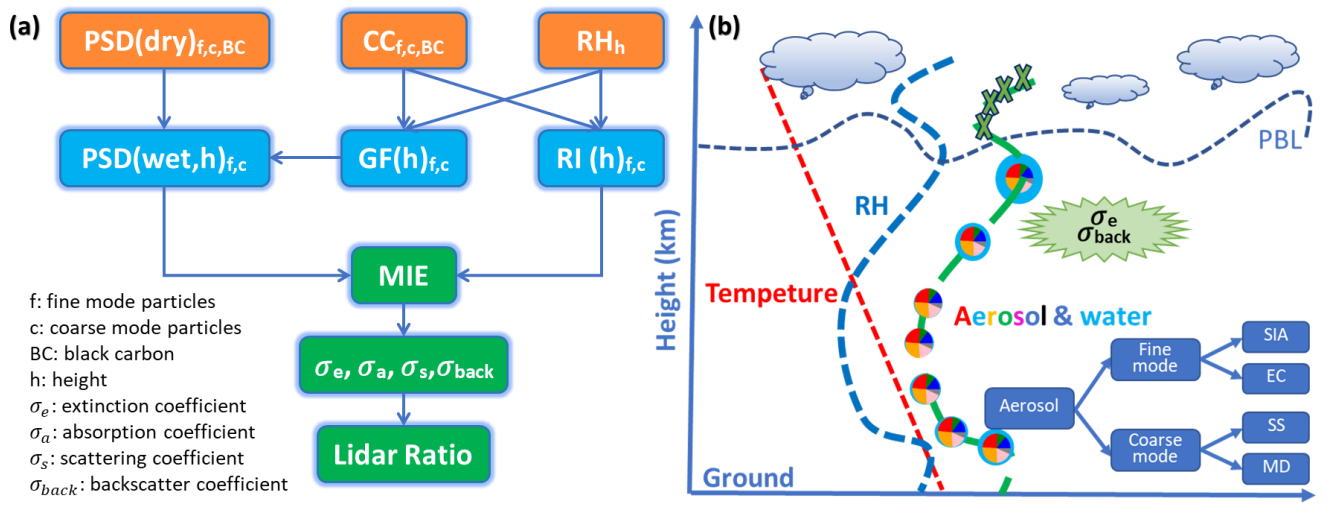### 2.3.2   CHM15k Ceilometer

The CHM15k ceilometer is a single-wavelength elastic-backscatter lidar manufactured by Lufft (2019), Germany. The CHM15k employs a Nd:YAG narrow-beam microchip laser that emits 1 ns pulses at a wavelength of 1064 nm, with a repetition rate ranging between 5-7 kHz and a receiver field of view of 450 µrad. The laser sensor is capable of measuring heights up to 15 km, with an initial overlap point of 80 m and complete overlap achieved at 800 m above ground (Hervo et al., 2016; Brunamonti et al., 2021). Wiegner and Geiss (2012) reported a relative error of 10% in backscatter coefficient at 1064 nm retrieved through this methodology using a similar system (CHM15kx by Jenoptik, Germany). The data used in this study were processed by the Eumetnet E-PROFILE ALC data hub: https://www.eumetnet.eu/activities/observations-programme/current-activities/e-profile/. The calibrated data with a vertical resolution of 30 m, and a time resolution of 5 minutes can be requested from the KNMI Data Platform (https://dataplatform.knmi.nl/). The ceilometer data was primarily used to aid in the visual discrimination between lofted aerosol layers (possibly from long range transport) and the boundary layer aerosols from recent mixing processes. An overview of the CHM15k measurement with the marked CAELI Raman lidar measurements times (from May 2021 to October 2021) is given in Figure1. Figure 2 presents the results of ceilometer measurements from May to October in 2021 with the color scale representing the intensity of the attenuated backscatter signal with the white regions (high intensity) generally correspond to clouds or fog. The orange vertical dashed lines mark the dates on which we conducted the Raman lidar measurements.
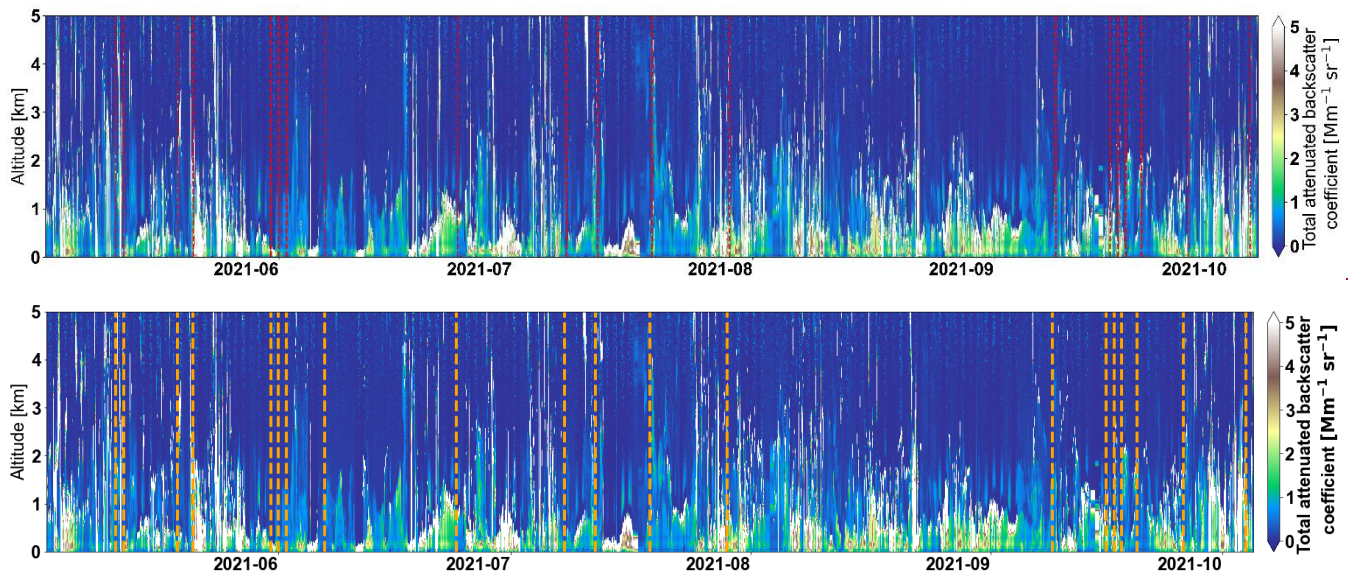
Figure 2: Backscatter coefficient at 1064 nm of CHMk15 ceilometer measurements at CESAR site from May to November in 2021. The ~~red~~orange dash lines represent the CAELI measurements availabilities.

2.4 Calculations

i: individual compound
ρ_i: density
RI_i: refractive index
K_i: Kappa value
h: height
PSD: particle size distribution
CC: chemical composition
V: volume fraction

f: fine mode particles
c: coarse mode particles
RH: relative humidity
Tem: temperature
σ_e: extinction coefficient
σ_a: absorption coefficient
σ_s: scattering coefficient
σ_{back}: backscatter coefficient

9

Figure 3: ~~The~~(a) the **flow diagram of the calculations**~~,~~, (b) a sketch of the vertical optical properties' calculations.

The aerosol optical properties (including the scattering coefficient, absorption coefficient, extinction coefficient, backscatter coefficient, and lidar ratio) were calculated based on Mie theory as displayed in the Figure ~~2,~~3(a). The main measurement data inputs were: (i) Chemical composition measured by the ACSM and MAAP as described in the section 2.1.1. (ii.) PSD measured by the MPSS and APS as described in the section 2.1.2. (iii.) RH and temperature profiles obtained from the ECMWF as described in the section 2.2.

The PSD was derived by combining data from both the MPSS and the APS, as detailed in Section S1 of the supplementary materials. Starting with the dry aerosol, the PSD data was then separated into fine mode ($< 2.5\,\mu m$) and coarse mode ($> 2.5\mu m$). We assumed that the fine mode was composed of an internal mixture of secondary inorganic aerosol (SIA) including ammonium, nitrate and sulphate, and organics, and that BC was externally mixed. The particle size distribution of BC is derived by multiplying its volumetric proportion within $PM_{2.5}$ by the overall fine particle size distribution. In addition, we assumed that the coarse mode was composed of sea salt (SS) and mineral dust (MD) ~~(Schaap et al., 2010)~~(Schaap et al., 2010). Because the coarse mode chemical composition was not measured during the RITA campaign, we employed the average SS and MD fractions obtained from the previous Trolix campaign in 2019[8], which indicated ~~a~~an average composition of 70% SS and 30% MD in volume fraction. The used densities of the SS and MD are listed in Table ~~S3~~1 and calculation details are in the supplementary materials section ~~S8~~S3. In addition, we conducted a sensitivity analysis by considering two extreme scenarios: one where the coarse mode was entirely composed of SS and another where it was entirely composed of MD. The outcomes of these sensitivity tests will be elaborated upon in the subsequent discussion. A uniform chemical composition was assumed for fine and coarse mode, respectively.

---

[8] https://ruisdael-observatory.nl/trolix19-tropomi-validation-experiment-2019/

The refractive index (RI) of the ~~SIA~~ fine ~~mode~~ and ~~the~~ coarse mode was calculated as volume-weighted average of the RI of the individual ~~constituents~~species (RI$_s$) (as shown Table ~~S3). The volume of each species was calculated as the measured~~ 1).

$$RI = \sum_s RI_s \frac{M_s}{\rho_s},\tag{1}$$

where M$_s$ is the mass concentration ~~divided by~~of species s and ρ_s is the corresponding density, ~~also~~shown in Table ~~S3.~~ 1. The RI used for BC is given in table 1.

Given the ~~PSD, as well as~~PSDs and the ~~RI~~RIs of the dry ~~aerosols~~SIA fine mode, coarse mode and BC, a Mie model (PyMieSca v1.7.5; (Sumlin et al., 2018)) was used to calculate the aerosol optical properties, namely the aerosol scattering coefficient, backscatter coefficient, extinction coefficient and lidar ratio at the wavelengths of the Nephelometer. The calculations were compared to the measured scattering coefficient and backscatter coefficient ~~as discussed in section 3.1~~(see in section 3.1). Sensitivity studies show that the calculations of scattering, backscatter and extinction coefficient are not very sensitive to the assumed BC size distribution.

~~For the ambient aerosol, we followed the same strategy to separate the fine mode and coarse mode as described for the dry aerosols, i.e. separate growth factors are derived for fine (only for SIA because BC was considered as non-hygroscopic) and coarse mode. The ambient PSD was calculated by multiplying the dry particle diameters with a diameter growth factor (GF) derived for the respective RH and temperature at different height above ground. Specifically, the GF for a given saturation ratio S (Gf(S)) is estimated based on kappa values (Zhang et al., 2017; Zou et al., 2019; Petters and Kreidenweis, 2007).~~

$$\sout{GF(S) = \left(\frac{K_{mix}S}{K_e - S} + 1\right)^{1/3},}\tag{1}$$

$$\sout{K_e = \exp\left(\frac{4\sigma M_w}{RT\rho}\right),}\tag{2}$$

For the ambient aerosol, a sketch of the calculation for the vertical optical profiles is given in Figure 2(b). In general, we followed the same strategy to separate the aerosols into SIA fine mode and coarse mode and externally mixed BC. A hygroscopic diameter growth factor (GF) is derived for fine (only for SIA because BC was considered as non-hygroscopic) and coarse mode separately. A ambient PSD was calculated by multiplying the dry particle diameters of fine and coarse mode with a diameter GF derived for the respective RH and temperature as a function of different height (j) above ground.

$$PSD_{ambient} = PSD_{dry}GF(S_j).\tag{2}$$

where the GF at each altitude j with given saturation ratio (S$_j$), is estimated using kappa values (Zhang et al., 2017; Zou et al., 2019; Petters and Kreidenweis, 2007).

$$GF(S_j) = \left(\frac{K_{mix}S_j}{K_{ej} - S_j} + 1\right)^{1/3}\tag{3}$$

with

$$K_{ej} = \exp\left(\frac{4\sigma M_w}{RT_j\rho}\right)\tag{4}$$

11

where the K_{mix} is the volume weighted average of the individual kappa values of the compound classes listed in the Table S3. For SIA, upper and lower limits (0.5-0.7) were used and accounted for in the uncertainty of the calculated optical properties. ~~K_e is essentially a constant at a fixed~~K_{ej} depends on temperature~~, where~~ T, which varies with altitude. σ is the surface tension of the solution/air interface (here we assume σ = 0.072 J m^{-2}), M_w is the molecular weight of water (M_w = 18 g mol-1), R is the universal gas constant (R = 8.3145 J mol^{-1} k^{-1}), T (K) is temperature, ρ is the density of water (ρ = 1000 kg m^{-3}). ~~With~~This results in two externally mixed, ambient size distributions for the fine mode: black carbon retains the original dry size distribution, and the ambient size distribution of SIA depends on the RH.

Given the GF at height j, the total water volume concentration can be obtained from the difference between the wet integral particle volume size distribution and the dry integral particle volume size distribution based on the following equation:

$$\cancel{V_{H2O}}V_{H2Oj} = \sum_i \frac{\pi D_{dryi}^3}{6}(\cancel{GF^3}GF_j^{\ 3} - 1)dn_i,$$

$$\cancel{(3)}(5)$$

where the dn_i is the number concentration (cm^{-3}) of size bin (i) and D_{dry} is the corresponding dry particle diameter (nm). The wet RI for the coarse and the fine mode was calculated as the volume weighted average of the individual RIs of all chemical constituents, now including the calculated water volume concentration in addition to the original volume concentrations. Finally, the optical properties of the ambient aerosol were calculated based on the Mie model with ambient ~~PSD~~RIs and ~~RI~~PSDs as input parameters. The vertical profiles of ~~the optical properties~~RIs and PSDs were derived by using the corresponding meteorological profile (RH and temperature) with the assumption of a homogenous distribution of the aerosol within the boundary layer height~~.~~ as sketched in Figure 3(b). The vertical profiles predicted by the model were compared with the Raman lidar measurements in the following section 3.2.

We quantified ~~calculation~~ uncertainties by assessing a set of nine parallel experimental results. These results were obtained ~~through cross-testing, specifically~~ by varying two key parameters as mentioned in the previous content: the volume fraction of SS and MD with values of 1, 0.7, and 0; and the SIA kappa values of 0.5, 0.6, and 0.7. The standard deviation of these parallel results serves as calculation uncertainties.

Table 1 The Refractive index, density and kappa values of the chemical composition. The values follow [a] Zou et al. (Zou et al., 2019), [b] Düsing et al. (2021), [c] Di Biagio et al. (2019), [d] Bi et al.(2018), Di Biagio et al.(2019), Zieger et al.(2017).

Chemical composition	RI (refractive index)	Density (g cm-3)	k
SIA	1.53 + 1e-6j	1.75	0.5-0.7
OA	1.47+0.02j[b]	1.40[a]	0.1[b]
BC	1.75+0.55j[b]	1.80[b]	0.0[b]
MD	1.56+0.006j[c]	2.65[e]	0.0[e]
SS	1.5+0.00j[d]	2.07[f]	1.1[f]
H$_2$O	1.333+0.00j[a]	1.00[a]	-

3   Results and discussion

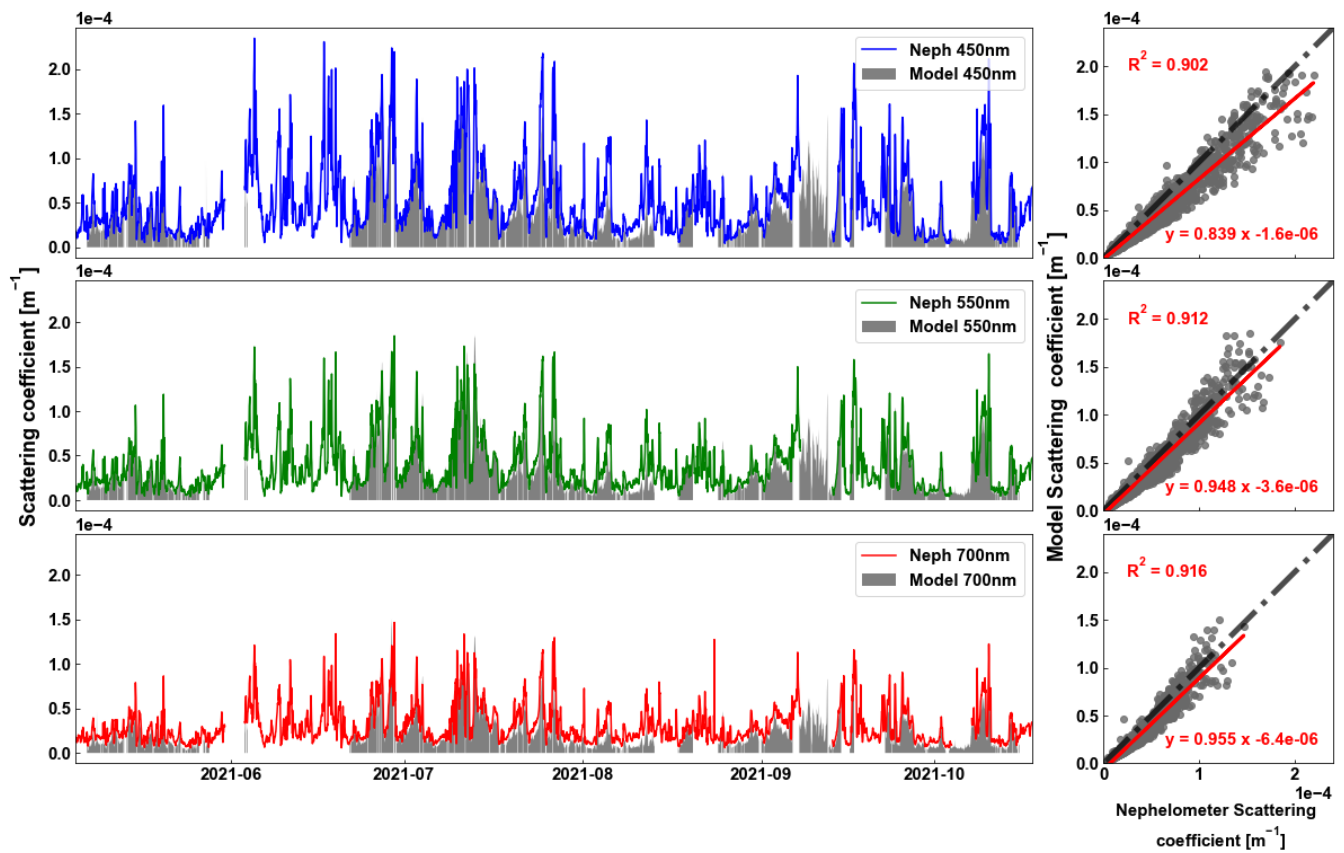## 3.1   Optical properties compared by calculation and Nephelometer at ground level

13
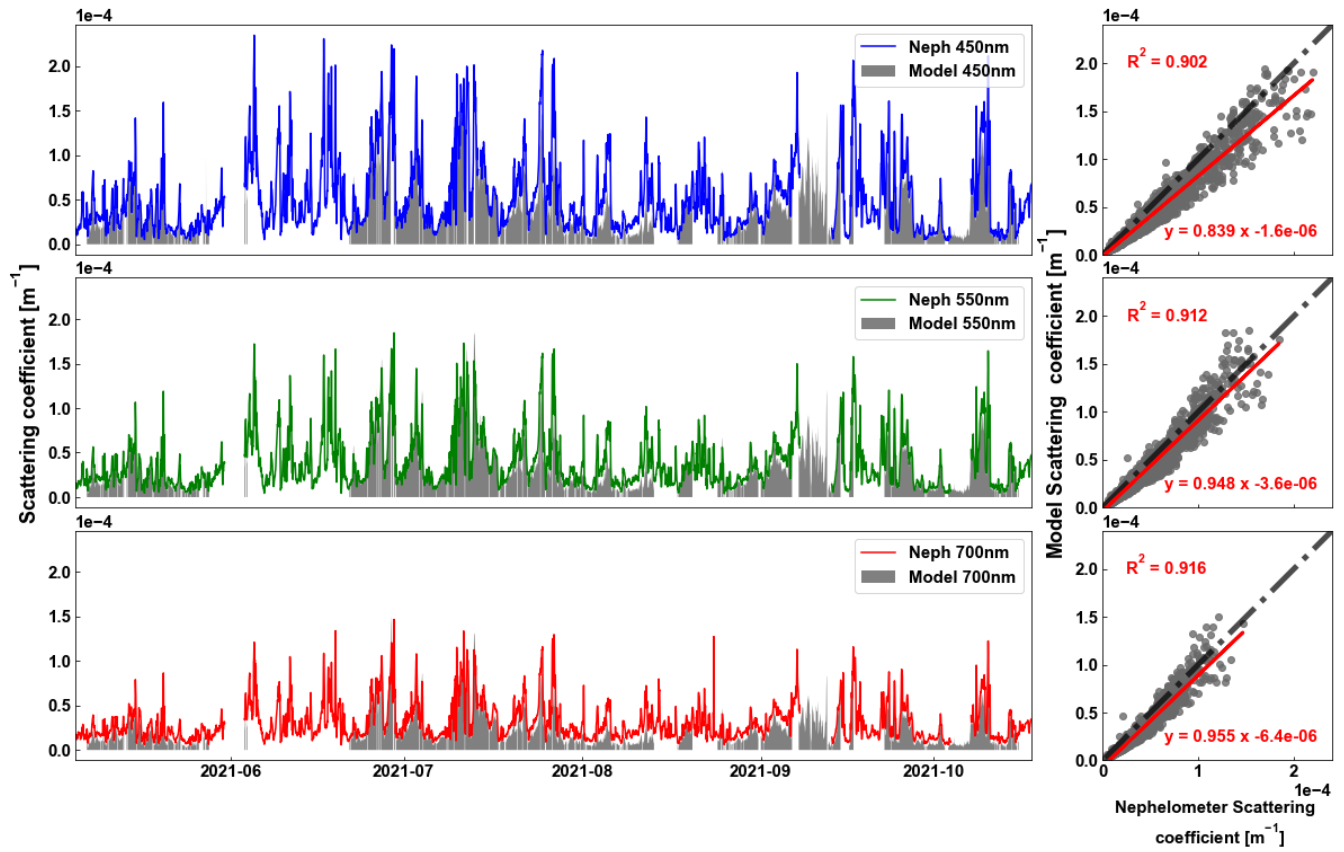
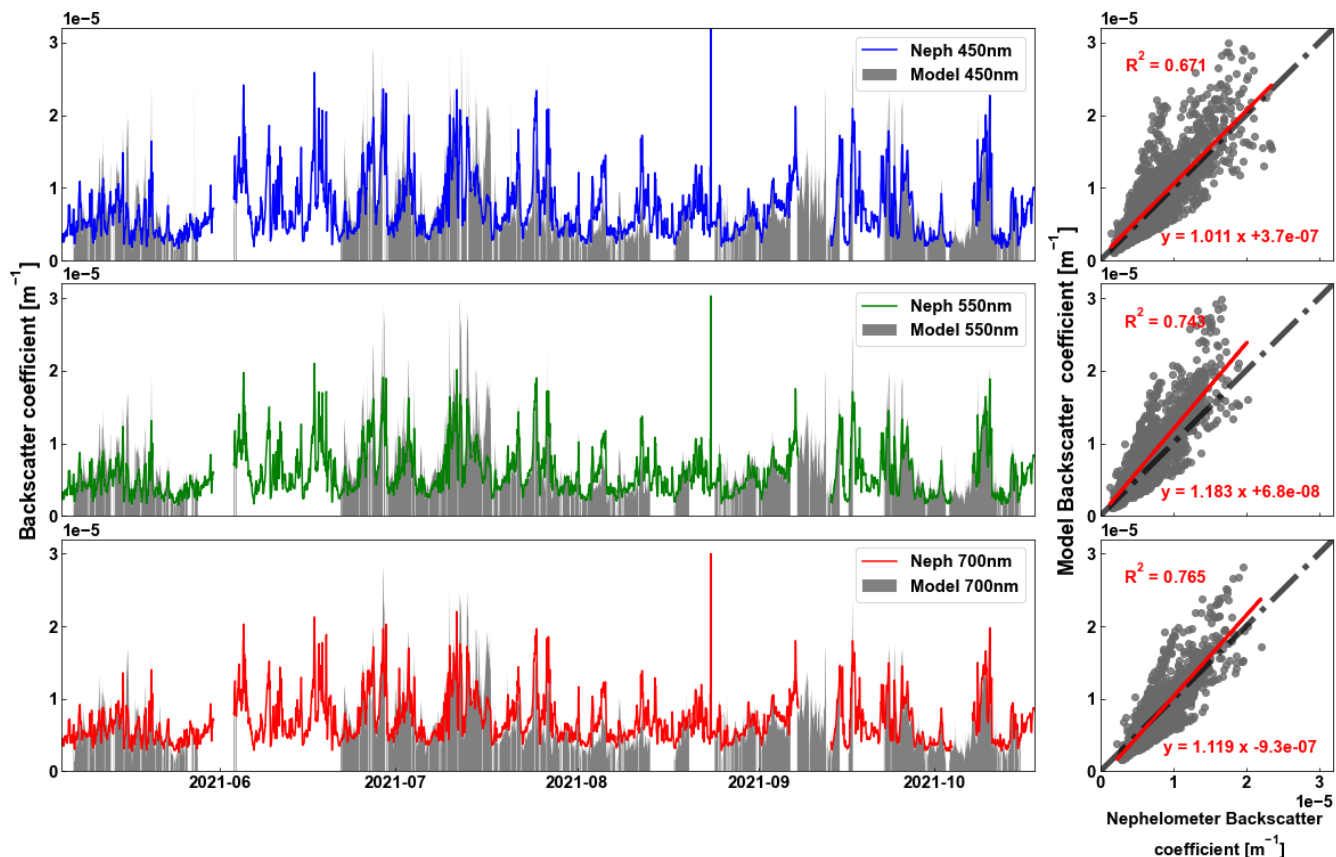**Figure 4: Time series of the scattering coefficient at 3 wavelengths (450nm, 550nm 700nm from the top to bottom, respectively) measured by the Nephelometer (coloured lines) and calculated from the Mie model (grey shades) in the left panel; a scatter plot of each wavelength between the measured scattering coefficient (horizontal axis) and the calculated scattering coefficient (vertical axis) in the right panel. The red line represents the regression line, and the black dashed line represents the 1:1 line.**

325

14

Figure 5: Time series of the backscatter coefficient at 3 wavelengths (450nm, 550nm 700nm from the top to bottom, respectively) measured by the Nephelometer (coloured lines) and calculated from the Mie model (grey shades) in the left panel; a scatter plot of each wavelength between the measured backscatter coefficient (horizontal axis) and the calculated scattering coefficient (vertical axis) in the right panel. The red line represents the regression line, and the black dashed line represents the 1:1 line.

The Nephelometer (at 450 nm, 550 nm, 700 nm) was operated continuously for measuring the aerosol scattering coefficient and backscatter coefficient at RH below 40%. Data from May to the end of October during the RITA-2021 campaign were used to validate the model calculations. ~~Figure 3 and~~ Figure 4 and 5 show the time series of the scattering coefficient and backscatter coefficient at 3 wavelengths obtained by Nephelometer measurements and the calculations outlined in section 2.4. The corresponding scatter plots including best fit lines are given on the right. Gaps in the calculated data are mainly due to maintenance and power failures of the aerosol in situ instruments, but the data coverage is more than 90%. Good agreement was found between the measured and calculated scattering coefficients, with a slope of 0.84 ($R^2 = 0.90$) for 450 nm, and 0.95 ($R^2 = 0.91$) for 550 nm, as well as 0.96 ($R^2 = 0.92$) for 700 nm. The model slightly underestimated the measurements, but the difference becomes smaller at larger wavelengths. Good agreement was also found for the backscatter coefficient, with the slope of the calculated values vs the measured values given as 1.01 ($R^2 = 0.67$) for 450 nm, and 1.18 ($R^2 = 0.74$) for 550 nm, as well as 1.12 ($R^2 = 0.77$) for 700 nm. The model calculations shown in the Figure ~~3~~4 and Figure ~~4~~5 assume that the coarse mode is composed of 70% SS and 30% MD as described in section 2.4. Results from a sensitivity study assuming that the

15

coarse mode consisted either entirely of SS or entirely of MD are presented in ~~Figure S6 and Figure S7~~Table S1 in the supplementary materials, and are very similar to the results in Figure ~~3 and Figure~~ 4 and Figure 5. More specifically, under the given particle size distribution conditions, the scattering coefficients for these two extreme scenarios differ on average less than 4% across varying wavelengths, the backscatter coefficients less than 19%. This shows that the backscatter coefficient is more sensitive to the coarse mode chemical composition, which can explain the lower R^2 values in Figure ~~4~~5 compared to Figure ~~3~~4. However, in general an average chemical composition of the coarse mode for the site is sufficient to predict the optical properties with reasonable accuracy. This is a considerable advantage, as the coarse-mode chemical composition is usually not as readily available as the fine mode composition for many sites. For sites, where the coarse mode comprises a very high mass fraction of PM_{10}, a more accurate representation of the coarse mode chemical composition might be necessary to predict the backscatter coefficient.

3.2   Comparison between the ~~modelling~~predicted ambient profiles and Raman lidar retrievals

The time periods when the CAELI Raman lidar was operated are marked in Figure 1. Due to unsuitable weather conditions, e.g. shallow atmospheric boundary layer or low clouds layers, it was not possible to retrieve lidar profiles for all time periods. Table S1 summarizes which in-situ data were available on the dates of the Raman lidar measurements. ~~Four~~Three representative examples ~~(~~, comprising two polluted cases and ~~two~~one clean ~~cases)~~case, were selected ~~and are discussed in detail~~for detailed discussion in the ~~following~~subsequent section. ~~The rest of the profiles are displayed~~Additional brief discussions on four more cases are provided in the supplementary ~~material section 6.~~materials.

3.2.1 Polluted cases

From 2021-05-19T20:00:21Z to 2021-05-19T20:53:07Z
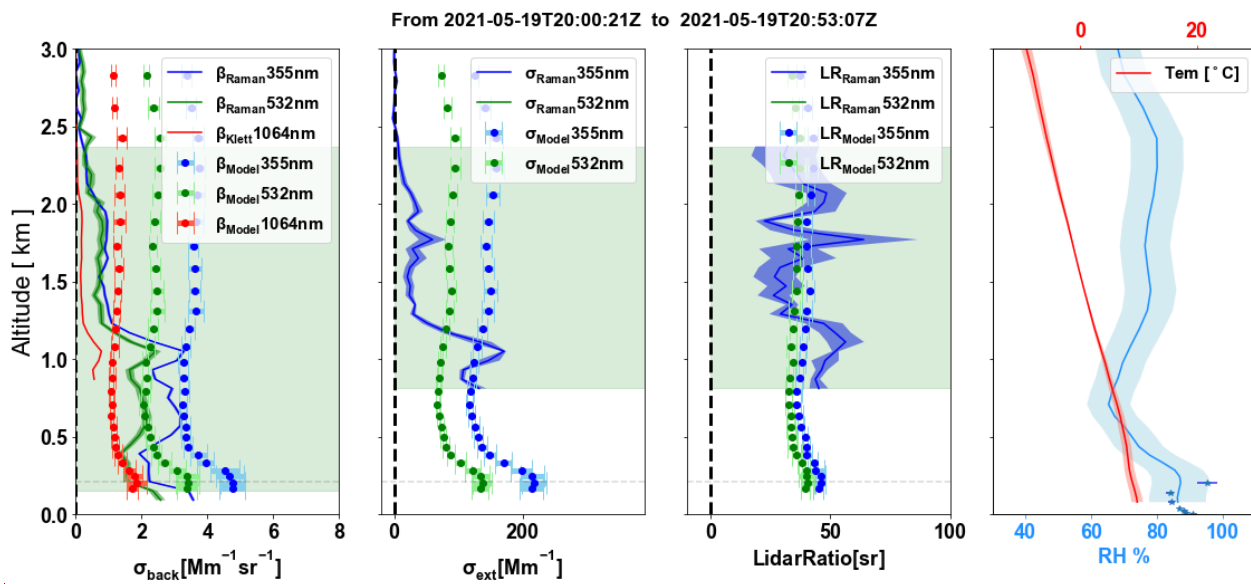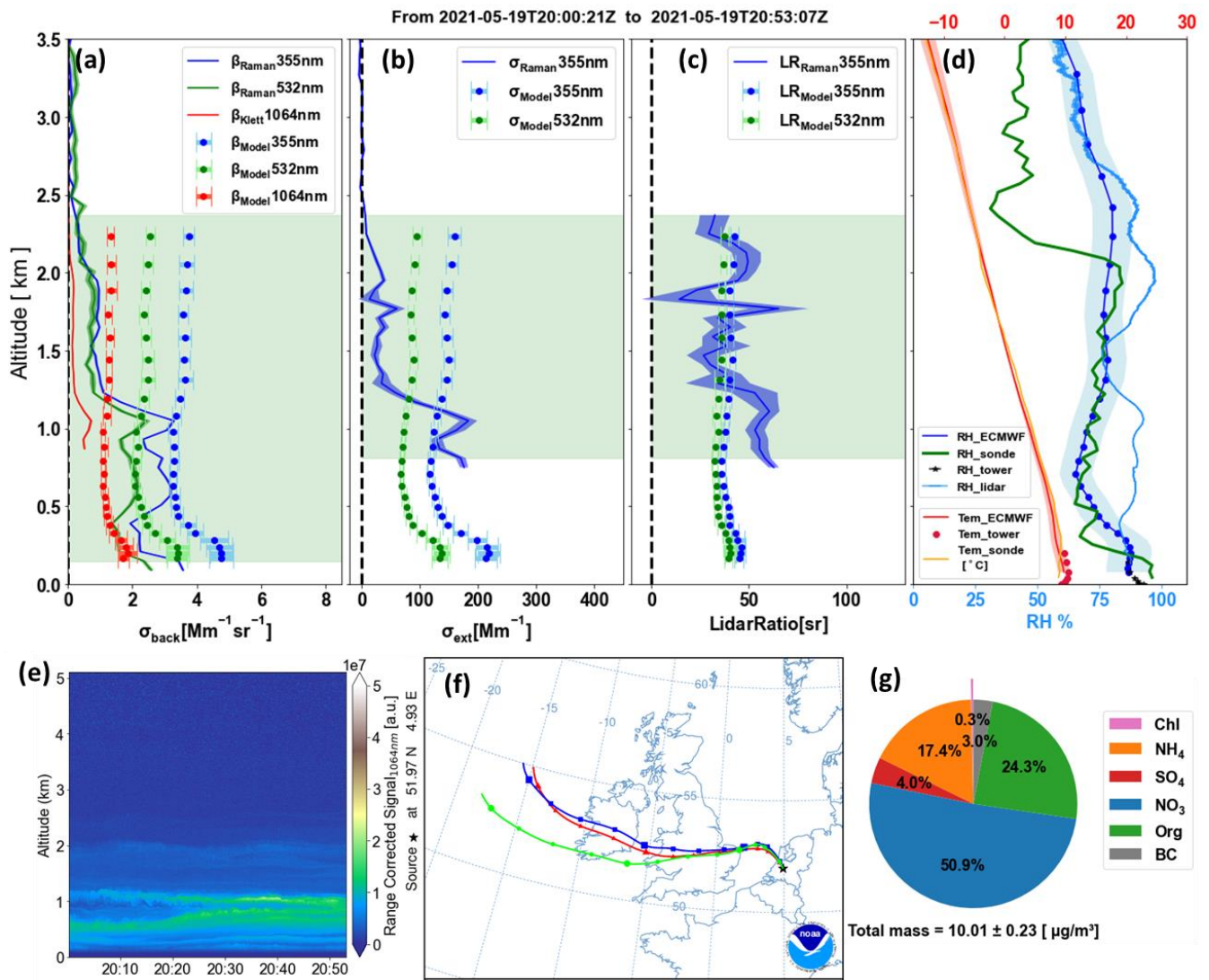
Figure 6: Vertical profiles of the aerosol optical properties (a) the Raman lidar backscatter coefficients (σ_{back}) at 355 nm (blue line),
532 nm (green line), and 1064 nm (using the Klett method; red line). The uncertainties of the measurements are given by the shaded
areas. The ~~predicted~~ backscatter coefficient ~~given~~predicted by the Mie ~~model~~calculations at 355 nm (blue dots), 532 nm (green dots),
and 1064 nm (red dots) with error bars representing the ~~model~~ corresponding uncertainties. (b) the ~~corresponding~~ extinction
coefficient (σ_{ext}) profiles of the lidar measurements and ~~model calculations.~~predictions. (c) the corresponding ~~retrieved~~lidar
measured and calculated lidar ratio profiles. The light green background represents upper and lower limits of the valid lidar
measurements. ~~The grey dashed horizontal line represents the lowest layer appearance.~~ in plots (a, b and c). (d) The vertical profiles
of the ~~meteorological data with RH in blue,~~RH% and temperature ~~in red, as well as the~~from ECMWF, from Raman lidar, from
tower in situ ~~measured RH (blue stars). Data from~~ (between 20:00~~:~~ and 21:00) and Radiosonde (launched from 23:30 to 23:46). (e)
**The 72 hours back trajectories at 100 (in red), 900 (in blue), 1600 (in green) meters during 20:00 to 21:00. (f) The CAELI Raman
lidar Range-corrected signal (RSC) at 1064nm during 20:00 to 20:53**~~:07 at~~. (g) Mass fractions of the chemical composition during
20:00 to 21:00. All data is in UTC time on May-19-2021.

Figure ~~5 shows~~6 presents the case from 20:00:21 to 20:53:07 (UTC) on May 19, 2021. It includes averaged vertical profiles

of ~~the~~ aerosol optical properties ~~retrieved~~obtained from ~~the~~ Raman lidar ~~during the period of 20:00:21 to 20:53:07 (UTC) on~~

18

~~May 19 2021. The 10-min~~retrievals and model calculations, 72-hour backward trajectories from three altitudes (100 m, 900 m, and 1600 m), the high-resolution Raman lidar measurements at 1064 nm, and the chemical composition from ground

380   measurements ~~were averaged~~. To clarify, the specified time period pertains to ~~best represent the lidar start and stop times, in this~~the lidar data; for the remaining datasets, the closest time range was selected based on their respective temporal resolutions. In particular ~~case from 20:00~~, the radiosonde, typically launched once daily around midnight, in this instance recorded a vertical profile from 23:30 to ~~20:50. The meteorological profiles were given by the ECMWF model with 1-hour time resolution with an uncertainty of 10%. The~~23:46. Model uncertainties ~~provided in the model calculations correspond to the~~ represent the

385   standard deviation ~~of the~~across various sensitivity studies as explained in section 2.4. ~~The~~ The ECMWF profiles show an uncertainty of 10%. In addition, the valid lidar measurement levels are marked in green background in the Figure ~~5~~6. The lowest altitude for the backscatter coefficient is above 150 m, whereas the lowest altitude for the extinction coefficient and lidar ratio is ~~determined by the valid retrievable range~~810 m as described in section 2.3.1. Furthermore, the upper limits were manually selected to only include aerosols originating from the planetary boundary layer (including the residual layer, if

390   present) for all the profiles, excluding lofted layers possibly originating from long-range transport. All the subsequent profiles adhered to the same approach. In this case, the dataset spanning from 810 m to 2370 m was employed for subsequent lidar ratio calculations and comparison to the model calculations.
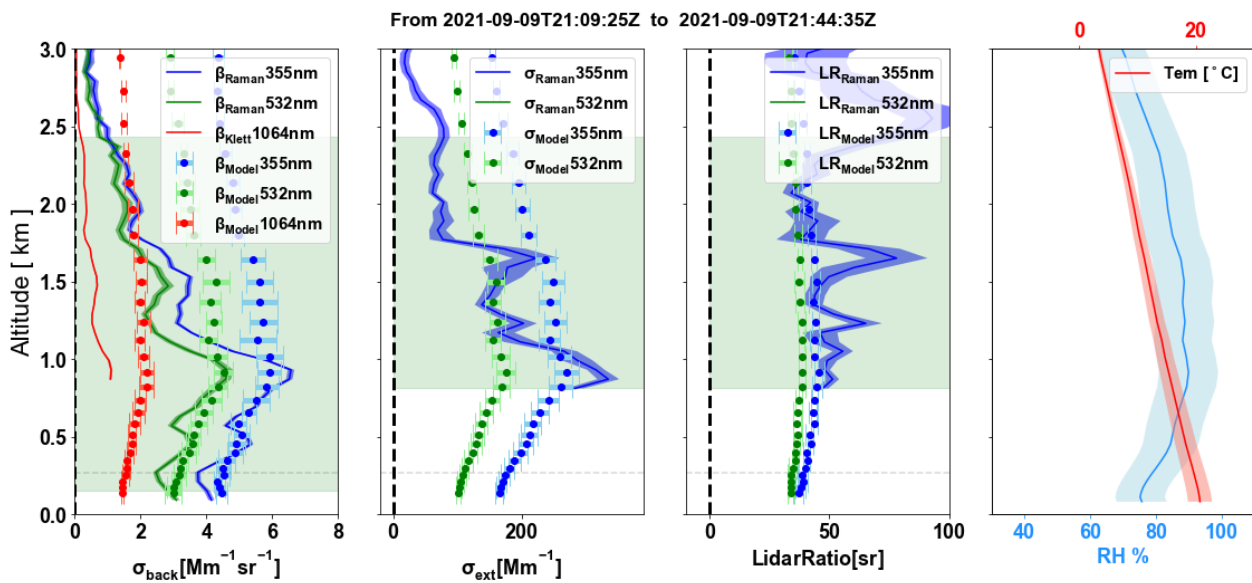
For this study case, ~~several aerosol layers were observed approximately below 1000 m, which can be seen in the~~ the Raman lidar image (~~in~~ Figure ~~S9). For the~~6(e)) shows that, at altitudes below approximately 1000 m, aerosols exhibit layers but they

395   are not distinctly pronounced. Therefore, the lidar retrieved backscatter ~~coefficient profiles, the simulated values are higher than the measured values below 500 m, which is likely due to inaccuracies in RH of the ECMWF data. This is highlighted by discrepancy between ECMWF data and situ RH measurements at 200 m as shown in the~~coefficients (Figure ~~5(d).~~6(a)) exhibit slight fluctuations in the vertical direction. Between the altitudes of 600 m and 1100 m the ~~backscatter coefficient does not change strongly with altitude and~~ retrieved and calculated backscatter coefficients agreed within 12%. Specifically, within this

400   range, the lidar reports values of 2.9 Mm^{-1} sr^{-1} for 355 nm and 2.0 Mm^{-1} sr^{-1} for 532 nm, comparable with calculated values of 3.3 Mm^{-1} sr^{-1} for 355 nm and 2.1 Mm^{-1} sr^{-1} for 532 nm. Below 500 m, the simulated values are higher than the measured values, which is probably partially due to higher values in RH of the ECMWF data compared to the radiosonde measurements in Figure 6(d), but potentially also due to the formation of a stable layer near the ground as shown by an increase of temperature with height in the tower data. Beyond 1100 m, the measured backscatter coefficients rapidly decrease to nearly 0 above the

405   mixed layer and the comparison with ground-based data ceases to be meaningful. ~~The Raman lidar image also shows increased backscatter values at around 1000 m, potentially indicating a different aerosol type or significant RH changes, which might not be well captured by the ECMWF data.~~ This case study demonstrates that ground-based measurements are not very well suited for estimating vertical profiles of extensive aerosol properties (such as the scattering coefficient) under conditions with poor mixing, which often occurs during evening and night-time.
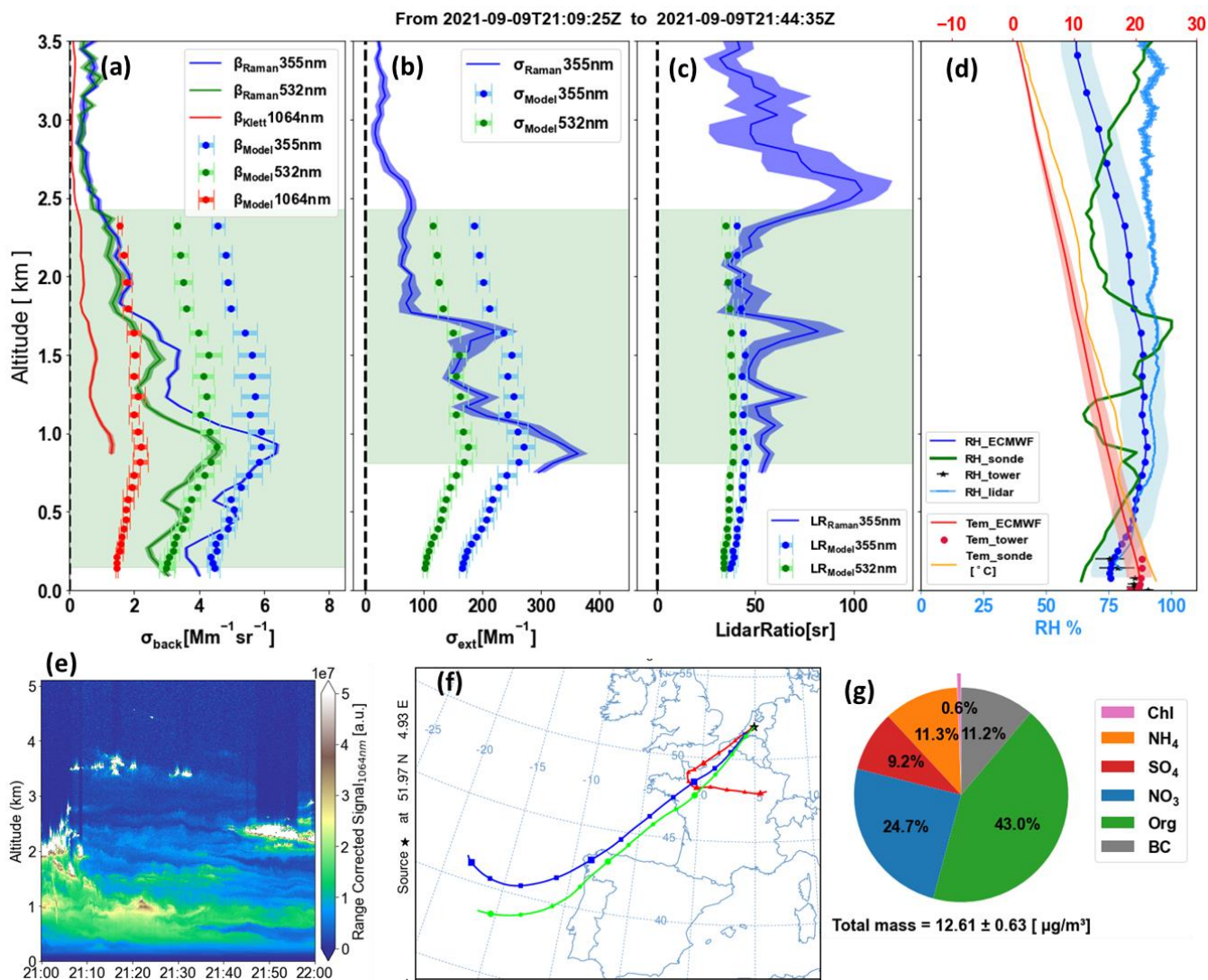
410   For the extinction coefficient profiles~~,~~ (Figure 6(b)), the Raman lidar retrievals provided good quality data only for 355 nm. A limited overlap existed between the valid lowest retrieved level and the aerosol layer at 1000 m, posing challenges for direct

19

comparisons. ~~Nevertheless, the~~The average extinction coefficient at 355 nm, ranging from 800 m to ~~1100~~1200 m, is approximately ~~110~~ Mm^{-1} ~~at 355 nm~~ for ~~both lidar measurements and the~~ calculations and slightly higher for retrievals, at about 145 Mm^{-1}.

415   Finally, the retrieved lidar ratio is ~~39~~45.1 ± 13.~~7 ± 10.6~~ sr^{-1} at 355 nm for the valid altitudes, whereas the calculations yield a lidar ratio of 40.1 ± 1.6 sr^{-1} at 355 nm and 35.3 ± 1.4 sr^{-1} at 532 nm~~.~~, as shown in Figure 6(c), showing relatively good agreement between calculations and retrievals. This range of values is typical for a polluted aerosol type (Bohlmann et al., 2018; Groß et al., 2013; Illingworth et al., 2015). ~~This classification is in line with ACSM measurements (refer to Figure S10), which indicate an average non-refractory PM~~$_{2.5}$ ~~mass concentration of 10.01 ± 0.23 µg m^{-3}. Notably, nitrate (50.9%) and ammonium (17.4%)~~

420   ~~contribute significantly to this mass concentration. Moreover, as shown in Figure S11, the analysis of back trajectory~~The 72-hour back trajectory analysis (Figure 6(f)) at three different altitudes using the Hysplit model (Stein et al., 2015; Rolph et al., 2017) implies that, the air masses originated from the sea, but were transported over Ireland and the United Kingdome and also the northwest of the Netherlands, resulting in elevated levels of anthropogenic pollutants. This result is in line with ACSM measurements (shown in Figure 6(g)), which indicate an average non-refractory PM$_{2.5}$ mass concentration of 10.01 ± 0.23 µg

425   m^{-3}. Notably, nitrate (50.9%) and ammonium (17.4%) contribute significantly to this mass concentration, which may reflect the substantial contributions from local nitrogen oxides and ammonia emissions to pollution in the Netherlands (Aan de Brugh, 2013).

From 2021-09-09T21:09:25Z to 2021-09-09T21:44:35Z

From 2021-09-09T21:09:25Z to 2021-09-09T21:44:35Z

Figure 7: Corresponding to Figure 5̶6 for the period from 21:09:25 to 21:44:35 at UTC time on Sep-09-2021.

Figure 6̶7 shows a̶the second polluted period̶case from 21:09:25 to 21:44:35 (UTC) on Sep-09-2021. The lowest layer was found around 270 m. The valid retrieval range is from 810 m to 2430 m. The Raman lidar images displayed in Figure S̶1̶2̶7(f) shows a complex and variable cloud structures during̶before and after this period. The profiles of backscatter coefficients (Figure 7(a)) obtained from Raman lidar retrievals and calculations agree remarkably well from the surface up to an altitude of 1000 m within the mixed layer height. On average, the differences between the two datasets are less than 5% for both 355 nm and 532 nm. Additionally, the backscatter coefficient profiles increased from the surface to 1000 m, from 3.9 to 6.5 Mm^{-1} Sr^{-1} for 355 nm and from 2.7 to 4.7 Mm^{-1} Sr^{-1} for 532 nm. This increase is reflected in all the RH profile̶profiles (from 75% to 90%̶)̶.% as displayed in (Figure 7(d)), including those from ECMWF, Raman lidar, tower, and radiosonde (2.5 hours later), which exhibit good consistency. The variations in aerosol optical properties within 1 km altitude were thus primarily due to

21

440   changes in ~~relative humidity~~RH and could be well predicted by ground-based data. However, the ground-based aerosol information is no longer applicable to profiles situated above 1 km.

The extinction coefficient profiles (Figure 7(b)) exhibit higher values initially at around 850 m, followed by a rapid decrease up to an altitude of approximately 1.2 km. The calculated extinction coefficient also decreases above 850 m but much less. ~~This could be partly due to the coarse resolution of the ECMWF RH profiles, but~~This most likely results from a lower aerosol

445   concentration above the mixed layer~~.~~, particularly during the latter part of the observation period showing in Figure 7(e). Those changes affect the average outcomes of lidar retrievals, resulting in lower values in the extinction profiles. Nevertheless, the extinction profiles of the measurements and calculations at 355 nm agreed reasonably well ~~in the altitude range of 900 m to 1000 m.~~with a height of about 1 km. Finally, the retrieved and calculated lidar ratios~~, which do not depend on the absolute aerosol concentration closely agree~~ (Fig. 7(c)) are in good agreement throughout the effective column range except around 1.5

450   km, indicating ~~a same~~the presence of similar aerosol ~~type~~types. The lidar average retrievals over the valid retrieval height yielded a value of ~~49~~53.1 ± 10.~~1~~8 sr^{-1}, while the model calculations produced a value of 43.2 ± 1.7 sr^{-1} at 355 nm. ~~Similar~~The analysis of 100m back trajectories, as depicted in Figure 7(f), demonstrated that the air masses originated from Central Europe, while air masses at higher altitudes (900m and 1600m) are shown to originate from the North Atlantic Ocean, and only the last day of the trajectories is very similar for all altitudes. Optical profiles based on ground-level data prove to be effective for

455   altitudes below 900 meters. Compared to the ~~lowest~~previous polluted case, the ACSM measurements showed a bit higher PM$_{2.5}$ mass concentration of 12.61 ± 0.63 µg m^{-3}, ~~primarily dominated by organic components (43%),~~ as illustrated in Figure ~~S13. Furthermore, the analysis of back trajectory, as depicted in Figure S14, demonstrated that the air masses originated from southern Europe.~~7(g). The main difference lies in the dominant contribution of organic components (43%).
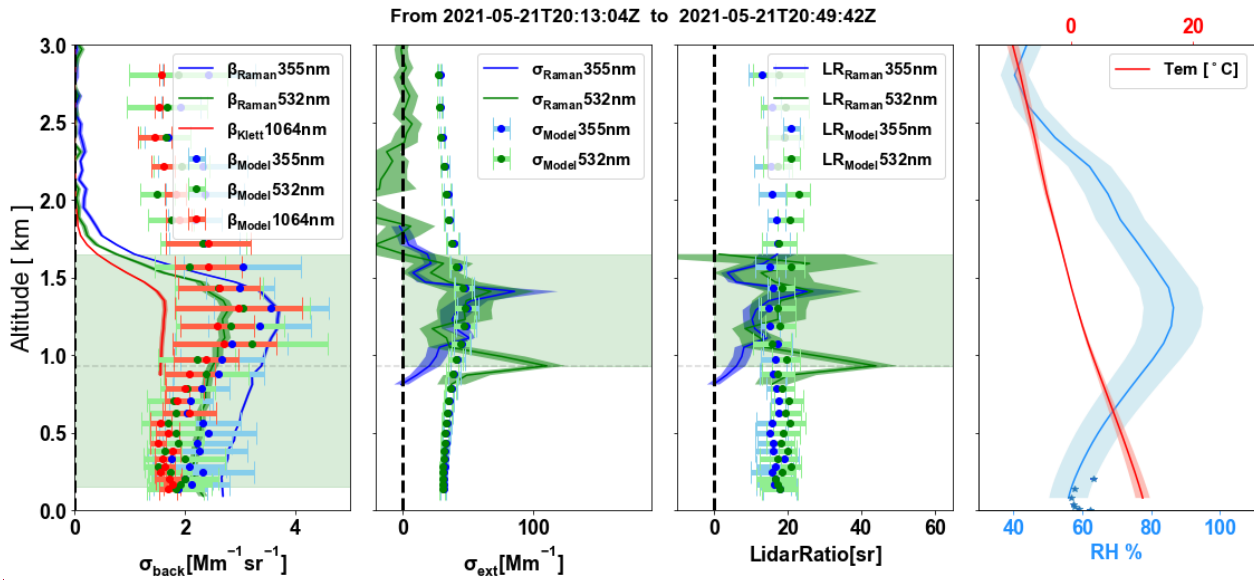
3.2.2   **Clean cases**

Figure 7: Corresponding to Figure 5 for the period from 20:13:04 to 20:49:42 at UTC time on May-21-2021.

Figure 7 shows the vertical profiles of the aerosol optical properties retrieved from the CAELI Raman lidar during the period of 20:13:04 to 20:49:42 (UTC) on May 21 2021. During the observed period, the PBLH was identified at an altitude of

465 approximately 1650 m, with the lowermost layer of valid extinction coefficient retrieval extending to around 930 m, as indicated in Figure S15. Within this altitude range, a good agreement is observed between retrievals and calculations for the backscatter coefficients at both 355 nm and 532 nm. Moreover, the retrievals illustrate a gradual increase in backscatter coefficients from the surface up to approximately 1.4 km altitude. Specifically, at 355 nm, the backscatter coefficient increases from approximately 2.7 $Mm^{-1}sr^{-1}$ to ~3.4 $Mm^{-1}sr^{-1}$ for 355 nm and from ~2.3 $Mm^{-1}sr^{-1}$ to ~2.4 $Mm^{-1}sr^{-1}$ for 532 nm as the RH

470 increases from around 50% at the surface to about 85% near the top of the PBLH. A similar increase in the calculated backscatter coefficient indicates that this increase is predominantly driven by aerosol hygroscopic growth. However, the calculated backscatter coefficient below 1 km was slightly lower than the retrievals, which might be due to the uncertainties in the RH profile. This is supported by Figure 7(d), where in situ RH measurements show a more pronounced RH increase above 200 m, whereas ECMWF observations increase less drastically. Furthermore, significant uncertainties are evident in the

475 model derived estimates. In this case, the coarse mode accounts for approximately 44% ± 6% of the total backscatter coefficient on average, and the assumption of the coarse mode being either pure SS or pure MD causes large uncertainties. The Raman lidar extinction coefficient and lidar ratio exhibit an anomalous spike at the onset of the valid retrieval height, which will be disregarded in the subsequent analysis and discussions. Within the altitude range of 1 km to 1.6 km, the model calculations closely matched the retrieved extinction coefficient on average. Notably, the profile of extinction coefficient at

480 355 nm and 532 nm showed a broad peak in the region of maximum RH, which was also captured by the model, further indicating that the variation with altitude was mainly caused by aerosol hygroscopicity growth. The average retrieved lidar

ratios are 11.5 ± 5.8 sr^{-1} for 355 nm and 18.1 ± 6.6 sr^{-1} for 532 nm, and the average calculated lidar ratios are 15.8 ± 1.0 sr^{-1} for 355 nm and 18.3 ± 1.8 sr^{-1} for 532 nm. These lidar ratios are typical for marine aerosols (around 5 to 30 sr^{-1}) (Bohlmann et al., 2018; Illingworth et al., 2015; Groß et al., 2013). The ACSM and MAAP measurements showed a very low PM$_{2.5}$ mass concentration with an average of 0.89 ± 0.07 µg m^{-3} during this period, and relative mass fractions of 27% organic aerosol, followed by 25.0% BC, 21.6% sulphate, 11.3% nitrate, 9.9% ammonium and 5.1% chloride as shown in Figure S16. While the ACSM is unable to measure NaCl, the presence of higher levels of chloride ions (below 1 % on average during the measurements) may suggest the existence of other chlorine-rich, inorganic salt particles. The back trajectory analysis as shown in Figure S17, further proved that the air masses originated from the sea with very clean background aerosols.

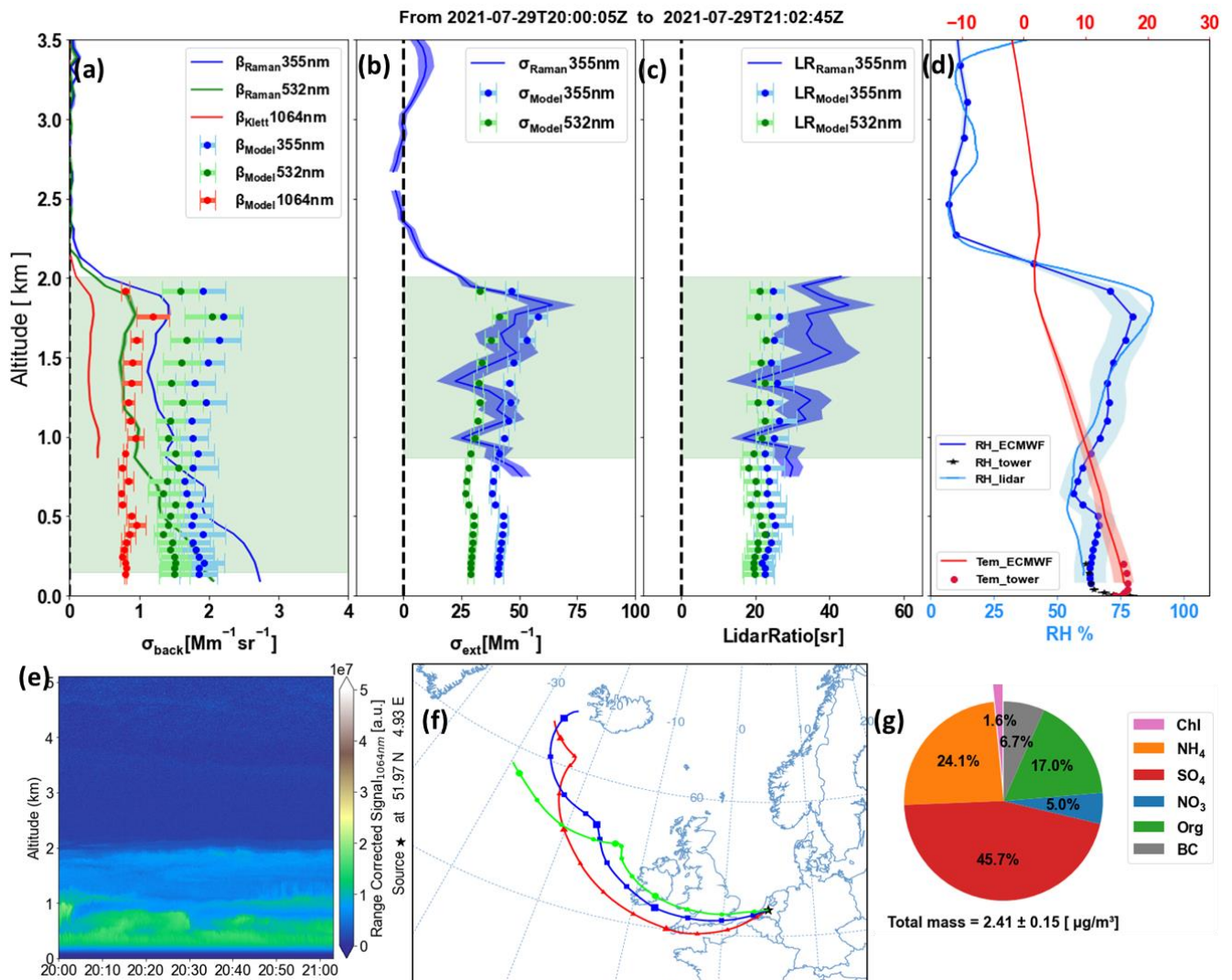From 2021-07-29T20:00:05Z to 2021-07-29T21:02:45Z
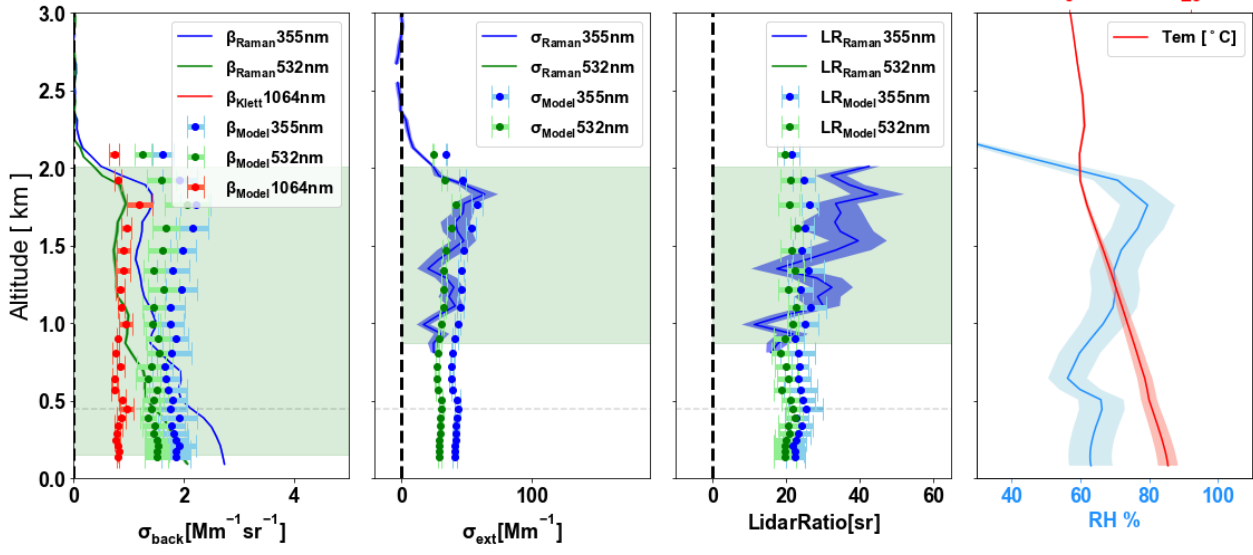
490

Figure 8: Corresponding to Figure 5~~6~~ for the period from ~~22~~20:00:05 to 21:02:45 at UTC time on July-29-2021.

Figure 8 shows the profiles for the period from the 20:00:05 to 21:02:45 (UTC) on July-29-2021. The ~~lowermost layer is situated at an altitude of approximately 450 m~~lidar image (Figure 8(e)) reveals two aerosol layers (below 1 km and 1-2 km) during this period, and the applicable range for the extinction profile and lidar ratio spans from ~~870~~810 m to 2010 m. ~~The~~Figure 8(a) shows that the retrieved backscatter coefficient decreases with altitude, but the calculated backscatter coefficient is rather constant with altitude. The calculations underestimate the retrievals at altitudes below 500 m and overestimate the retrievals (by approximately 20% - 30%) at altitudes around 1500 m. This difference can be attributed to (i) variations in aerosol concentrations or chemical properties between ground-level and higher altitudes; (ii) ~~a potentially inaccurate RH profile near the ground~~other inaccuracies in the model such as insufficient information on the size resolved chemical composition and aerosol mixing state; (iii) The RH profiles may be inaccurate, where the 1hr time resolution of the re-analysis data do not

capture correctly the development of a nocturnal stable layer near the ground; ~~(iii) other inaccuracies in the model such as insufficient information on the size resolved chemical composition and aerosol mixing state; (iv) on the other hand,~~As shown in Figure 8(d), below 200m, the RH values from ECMWF and the ground-based tower show good overlap. However, between 200m and 500m, the RH values calculated by the lidar and those from ECMWF by up to 10% RH. Due to the absence of direct measurement data (radiosonde data was unavailable on this day), it is challenging to ascertain which dataset is closer to the actual values. (iv) the lidar retrievals near the ground could also be inaccurate, especially at the low aerosol concentrations in this clean case. However, despite these discrepancies, the ~~model provided~~calculated values are on the order of magnitude of the retrievals and agree within uncertainties for a large part of the profile.

It is noticeable that the calculated backscatter values have larger uncertainties in this clean case than in the polluted cases. The main reason is that in the clean case the contribution of the coarse more to the backscatter coefficient is larger and thus the extreme assumptions regarding the chemical composition (pure sea salt vs pure mineral dust) starts to affect the results. Since sea salt has a much higher growth factor than mineral dust, the ambient size distribution of the coarse mode differs considerably, especially at high RH. Nevertheless, the resulting uncertainties of the backscatter coefficient are still in a reasonable range.

The agreement between the modelled and retrieved values of extinction coefficient (Figure 8(b)) and lidar ratio profiles (Figure 8(c)) within the altitude range of ~~900~~800 m to 1800 m suggests a reasonable representation of aerosol properties by the ground-based measurements throughout the boundary layer. Especially, the lidar ratio obtained from the Raman lidar measurements at 355 nm was ~~determined to be 30 ±~~ 31.8~~.3~~ ± 6.8 sr^{-1}, while the model estimated values were 25.0 ± 1.3 sr^{-1} at 355 nm and 21.5 ± 1.1 at 532 nm. These lidar ~~ratio values~~ratios are typical for marine aerosols (around 5 to 30 sr^{-1}) (Bohlmann et al., 2018; Illingworth et al., 2015; Groß et al., 2013). Results are consistent with aerosols originating from marine sources during the observed period, which is supported by the back trajectory shown in Figure ~~S20.~~8(f). Additionally, the low aerosol mass concentration (2.41 ± 0.51 µg m^{-3}) shown in Figure ~~S19~~8(g) with a significantly higher fraction of sulphate (45.7%) further supports this result.

~~There are 22 more profiles displayed in the supplementary material section 6, where it shows extinction and backscatter coefficients are sometimes severely under- or overestimated by the ground based calculations. However, the lidar ratios are much better predicted. We speculate that the main reasons for this phenomenon are as follows: Although upper-level aerosols may have similar chemical composition and size distribution as surface level aerosols, they may be present at different concentrations. Thus, the backscatter or extinction coefficients of aerosols may be overestimated or underestimated by the same factor resulting in a similar lidar ratio. Or it could be the meteorological data may not be sufficiently accurate. Especially when relative humidity is overestimated or underestimated, this has a more significant influence on extinction and backscatter coefficients, but its impact on the lidar ratio is less pronounced. Another crucial factor may be the influence of shape effects, which normally become more significant for the larger particles. Previous studies show that the backscatter cross section and extinction cross section may be underestimated or overestimated by a factor ranging from −2 to +5, depending on the particle shapes and size ranges (Potenza et al., 2016; Geisinger et al., 2017).~~

All remaining profiles marked in Figure 2 have been stored in a publicly accessible repository (DOI 10.5281/zenodo.11174464), available for interested readers. The results show extinction and backscatter coefficients are sometimes considerably under- or overestimated by the ground-based calculations. However, it is worth emphasizing that the lidar ratios are much better predicted. We speculate that the main reasons for this phenomenon are as follows: (i) the upper-level aerosols may have similar chemical composition and size distribution as surface-level aerosols, but are present at different concentrations. Thus, the backscatter or extinction coefficients of aerosols may be overestimated or underestimated by the same factor, resulting in a similar lidar ratio. (ii) Or it could be the meteorological data may not be sufficiently accurate. Especially when RH is overestimated or underestimated, this has a more significant influence on extinction and backscatter coefficients, but its impact on the lidar ratio is less pronounced. (iii) Another crucial factor may be the influence of shape effects, which normally become more significant for the larger particles. Previous studies show that the backscatter cross-section and extinction cross-section may be underestimated or overestimated by a factor ranging from -2 to +5, depending on the particle shapes and size ranges (Potenza et al., 2016; Geisinger et al., 2017).

3.3   Summary of the lidar ratio comparison
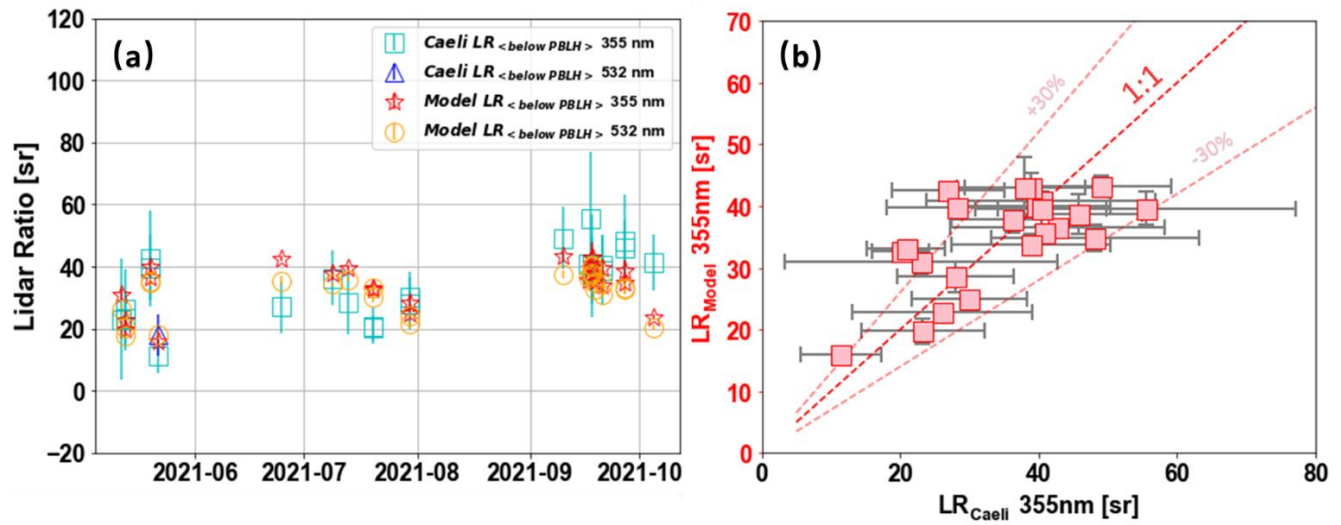
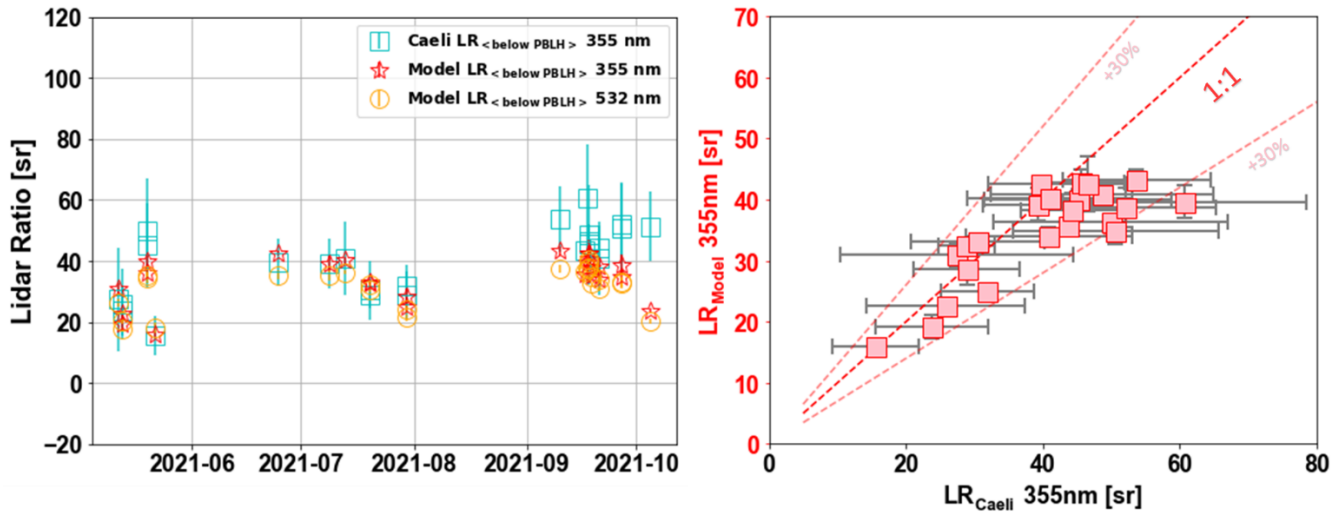## 3.3 Summary of the lidar ratio comparison

Figure 9: (a) Time series of the mean lidar ratio and its uncertainty (at 355nm and 532 nm) from the valid lidar retrievals and ~~model~~the calculations. (b) Scatter plot of the lidar ratios (LR) from Raman lidar measurements (x axis) and from calculations (y axis) at 355 nm.

Figure 9 (a) shows the time series of the average lidar ratios (at 355nm and 532nm) for each period retrieved from lidar measurements and calculated by the model for the corresponding valid retrieval levels of each profile. The error bars correspond to the standard deviation of each effective lidar ratio profile. For the most part, the ~~simulated~~predicted lidar ratios are comparable to the lidar ratios measured by Raman lidar~~.~~, however for retrieved lidar ratios above 50 sr, the predictions seem systematically lower. Significant standard deviations in Figure 9 (a) illustrate that the measured lidar ratios were quite variable across the planetary boundary layer, which might indicate different aerosol layers at various altitudes. This cannot be taken into account for the calculations. Consequently, the model-generated lidar ratios tend to remain relatively stable with altitude for the majority of cases. Nevertheless, the ~~simulated~~predicted lidar ratios are within the range of retrieved lidar ratios, with differences from case to case are usually smaller than ± 30% for the wavelength at 355nm as shown in Figure 9 (b). On the whole, the calculated lidar ratios were in the range of 16 - 43 sr at 355 nm and 18 - 41 sr at 532 nm on average, indicating a relatively low-pollution environment. Furthermore, the ~~model~~ calculations show that the lidar ratio has a small wavelength dependence, with on average higher lidar ratio at 355 nm (slope of 0.64 and R^2 of 0.94 between the lidar ratio at 355 nm and 532 nm). This is consistent with findings from Mattis et al (2004), which summarized a long-term Raman lidar measurements with the lidar ratio from 2000 to 2003 for central European haze, specifically the anthropogenic aerosol particles, with values of 58 ± 12 sr for 355 nm, 53 ± 11 sr for 532 nm, and 45 ± 15 sr for 1064 nm wavelengths in the upper part of the PBL. In the free tropospheric and stratospheric layers, the lidar ratio possibly has a different wavelength dependence, where Moritzet et al. (2004) reported that the lidar ratios were 40 - 45 sr for 355 nm, 65 - 80 sr for 532 nm, and 80 - 95 sr for 1064 nm.

29

In summary, ~~through the combination of ground-based aerosol~~by integrating data from in situ measurements with the readily accessible ECMWF data, we can predict aerosol optical properties ~~within the mixed layer relatively well. In particular, the lidar ratio can be predicted throughout~~to a certain extent when the aerosol mixing is homogeneous below the boundary layer ~~in~~. Such conditions are more likely during the day, but occur less often during the evening and night, when Raman lidar data are typically available. While not as sensitive as the ~~absence~~retrievals, the calculations are capable of capturing significant shape changes in the vertical distribution. Despite occasional overestimations and underestimations of ~~strong elevated~~backscatter and extinction values when assumptions deviate from actual conditions (i.e., homogeneous aerosol ~~layers,~~mixing), our predictions for the lidar ratio are very effective up to heights of about 2 km. This would allow estimating lidar ratios applicable to simple backscatter lidars from ground-based in-situ measurements. For such ~~as dust layers. However~~calculations, it is crucial for the model to be furnished with an accurate measured particle size distribution including the coarse mode. While possessing chemical insights into the coarse mode is an advantage, it is not absolutely necessary~~. However, the~~, as long as a typical composition can be assumed. In our case studies, we showed that the extreme assumptions of pure sea salt aerosols vs pure mineral dust aerosols for the coarse mode resulted in reasonable uncertainties ~~of the calculations might be significant~~in the predicted optical properties for coarse mode mass fractions about 49% on average (range from 14%-81%). This however, does not take into account the uncertainties regarding the shape of pure mineral dust aerosols, which could be considerable. Therefore, in regions ~~the coarse mode particles are dominant.~~dominated by dust aerosols the simple assumption of spherical particle shape might not be appropriate and could result in much larger bias. Within the mixed layer, our results show that the enhancement of the backscatter coefficient and extinction coefficient ~~is mainly driven by hygroscopicity~~strongly depend on the particle hygroscopic growth. Consequently, the availability of accurate and high vertical resolution RH profile is important for constructing a robust model input, but even one-hourly ECMWF humidity fields give reasonable results.

4   Conclusions

In this study, a Mie theory-based model was applied to ground-based in-situ measurements to predict ambient aerosol optical properties including scattering coefficient, backscatter coefficient, extinction coefficient and lidar ratio. The input data are: (i) aerosol chemical composition and (ii) particle size distribution measured at the surface; (iii) the meteorological data from European Centre for Medium-Range Weather Forecasts (ECMWF). The data was collected during the Ruisdael land-atmosphere interactions Intensive Trace-gas and Aerosol (RITA) ~~2021~~campaign, at the CESAR site in the Netherlands with a total time span of 5 months (from May to October in 2021). The calculations were first validated by comparing to observations from TSI integrating nephelometer at dry conditions for the entire period. The calculations and measurements across multiple wavelengths with slopes of 0.84 - 0.96 ($R^2 \geq 0.90$) for the scattering coefficients, and slopes of 1.01 – 1.18 ($R^2 \geq 0.67$) for the backscatter coefficients. Furthermore, the model was compared with aerosol optical vertical profiles retrieved by a multi-wavelength Raman lidar. The results showed that, for a homogeneously distributed aerosol within the mixing layer, the model

could effectively simulate the vertical profile of the aerosol backscatter coefficient as a function of ~~relative humidity within~~ ~~the mixed layer.~~RH which varies with altitude. The comparison of extinction coefficients posed challenges due to the limited overlap between the lower layer of retrievals and the mixed layer. However, the profiles at the shared levels exhibited a reasonable connection, suggesting a meaningful comparison could still be made. The simulated lidar ratio can predict the measured lidar ratio within ± 30% for the average values below the planetary boundary layer height. Overall, our study shows that, besides the particle size distribution and chemical composition, the relativity humidity is a crucial input for the model to generate accurate backscatter and extinction coefficient profiles. Moreover, in the well mixed boundary layer, it is usually possible to approximate the lidar ratio using ground-based measurements. This approach allows for the extension of extinction profiles to lower altitudes that are typically challenging to retrieve, or it can be employed alongside basic backscatter lidar systems to calculate the extinction and then further the aerosol optical depth, which could potentially extend to forecasting aerosol optical depth and could offer advantages in extensive-scale or worldwide radiation simulations.

Data availability

The most data involved in this study is part of the Ruisdael Observatory (https://ruisdael-observatory.nl) project. The ground based measurements can be accessed at repository under https://doi.org/10.5281/zenodo.7924288 ~~(Liu et al., 2023).~~(Liu et al., 2023a). The additional model and lidar profiles can be accessed at repository under https://doi.org/10.5281/zenodo.11174465 (Liu et al., 2024). The in situ meteorological data and Ceilometer data are available at the KNMI Data Platform (https://dataplatform.knmi.nl). Other remote sensing data can be accessed from the authors upon reasonable request.

Author contribution

XL, BH, and UD designed this study. DG, AA, AH, DD, UD and XL implemented the experiment and sample analysis. DG and AA provided the ~~LIDAR~~lidar retrievals. XL analysed the data and wrote the manuscript. All co-authors proofread and commented on the paper.

Competing interests

The authors declare that they have no conflict of interest.

Acknowledgements

References

Aan de Brugh, J. M. J.: Aerosol processes relevant for the Netherlands, Chapter 6 pp., 2013.ISBN: 9789461734211

Anderson, T. L. and Ogren, J. A.: Determining Aerosol Radiative Properties Using the TSI 3563 Integrating Nephelometer,
635 Aerosol Sci. Technol., 29, 57–69, https://doi.org/10.1080/02786829808965551, 1998.

Anderson, T. L., Covert, D. S., Marshall, S. F., Laucks, M. L., Charlson, R. J., Waggoner, A. P., Ogren, J. A., Caldow, R., Holm, R. L., Quant, F. R., Sem, G. J., Wiedensohler, A., Ahlquist, N. A., and Bates, T. S.: Performance Characteristics of a High-Sensitivity, Three-Wavelength, Total Scatter/Backscatter Nephelometer, J. Atmos. Ocean. Technol., 13, 967–986, https://doi.org/https://doi.org/10.1175/1520-0426(1996)013<0967:PCOAHS>2.0.CO;2, 1996.

640 Ansmann, A., Riebesell, M., and Weitkamp, C.: Measurement of atmospheric aerosol extinction profiles with a Raman lidar, Opt. Lett., 15, 746–748, https://doi.org/10.1364/OL.15.000746, 1990.

Ansmann, A., Riebesell, M., Wandinger, U., Weitkamp, C., Voss, E., Lahmann, W., and Michaelis, W.: Combined raman elastic-backscatter LIDAR for vertical profiling of moisture, aerosol extinction, backscatter, and LIDAR ratio, Appl. Phys. B Photophysics Laser Chem., 55, 18–28, https://doi.org/10.1007/BF00348608, 1992a.

645 Ansmann, A., Wandinger, U., Riebesell, M., Weitkamp, C., and Michaelis, W.: Independent measurement of extinction and backscatter profiles in cirrus clouds by using a combined Raman elastic-backscatter lidar, Appl. Opt., 31, 7113, https://doi.org/10.1364/ao.31.007113, 19921992b.

Apituley, A., Wilson, K. M., Potma, C., Volten, H., and Graaf, M. De: Performance Assessment and Application of Caeli — A high-performance Raman lidar for diurnal profiling of Water Vapour , Aerosols and Clouds, 8–11, 2009. https://ruisdael-
650 observatory.nl/cesar-observatory/istp8/data/1753005.pdf

Balis, D. S., Amiridis, V., Nickovic, S., Papayannis, A., and Zerefos, CBi, L., Lin, W., Wang, Z., Tang, X., Zhang, X., and Yi, B.: Optical propertiesModeling of Saharan dust layers as detected by a Raman lidar at Thessaloniki, Greece,Sea Salt Aerosols: The Effects of Nonsphericity and Inhomogeneity, J. Geophys. Res. Lett., 31, 10 13Atmos., 123, 543–558, https://doi.org/10.1002/2017JD027869, 2018.

655 Di Biagio, C., Formenti, P., Balkanski, Y., Caponi, L., Cazaunau, M., Pangui, E., Journet, E., Nowak, S., Andreae, M. O., Kandler, K., Saeed, T., Piketh, S., Seibert, D., Williams, E., and Doussin, J. F.: Complex refractive indices and single-scattering albedo of global dust aerosols in the shortwave spectrum and relationship to size and iron content, Atmos. Chem. Phys., 19, 15503–15531, https://doi.org/10.1029/2004GL019881, 20045194/acp-19-15503-2019, 2019.

Bhardwaj, A., Sam, L., Bhardwaj, A., and Martín-Torres, F. J.: LiDAR remote sensing of the cryosphere: Present applications and future prospects, Remote Sens. Environ., 177, 125–143, https://doi.org/10.1016/j.rse.2016.02.031, 2016.

Bohlmann, S., Baars, H., Radenz, M., Engelmann, R., and Macke, A.: Ship-borne aerosol profiling with lidar over the Atlantic Ocean: From pure marine conditions to complex dust-smoke mixtures, Atmos. Chem. Phys., 18, 9661–9679, https://doi.org/10.5194/acp-18-9661-2018, 2018.

François Marie Bréon , F.-M.: How Do Aerosols Affect Cloudinessdo aerosols affect cloudiness and Climate?.Science313,climate?, Science (80-.)., 313, 623– 624., https://doi.org/10.1126/science.11316681131625, 2006.

Brunamonti, S., Martucci, G., Romanens, G., Poltera, Y., Wienhold, F. G., Hervo, M., Haefele, A., and Navas-Guzmán, F.: Validation of aerosol backscatter profiles from Raman lidar and ceilometer using balloon-borne measurements, Atmos. Chem. Phys., 21, 2267–2285, https://doi.org/10.5194/acp-21-2267-2021, 2021.

Chang, G. C., Dickey, T., and Lewis, M.: Toward a Global Ocean System for Measurements of Optical Properties Using Remote Sensing and In Situ Observations, Remote Sensing of the Marine Environment: Manual of Remove Sensing.,Chapter: 9, 305-346, 2006Sens. Mar. Environ. Man. Remote Sens., 6, 305–346, 2006. http://opl.ucsb.edu/html-old/tommy/pubs/ChangetalManRemSens06.pdf.

Cooney, J., Orr, J., and Tomasetti, C.: Measurements Separating the Gaseous and Aerosol Components of Laser Atmospheric Backscatter, Nature, 224, 1098–1099, https://doi.org/10.1038/2241098a0, 1969.

Collis, R. T. H. and Russell, P. B.: Lidar measurement of particles and gases by elastic backscattering and differential absorption BT - Laser Monitoring of the Atmosphere, edited by: Hinkley, E. D., Springer Berlin Heidelberg, Berlin, Heidelberg, 71–151, https://doi.org/10.1007/3-540-07743-X_18, 1976.

D'Amico, G., Amodeo, A., Baars, H., Binietoglou, I., Freudenthaler, V., Mattis, I., Wandinger, U., and Pappalardo, G.: EARLINET Single Calculus Chain-overview on methodology and strategy, Atmos. Meas. Tech., 8, 4891–4916, https://doi.org/10.5194/amt-8-4891-2015, 2015.

Dawson, K. W., Meskhidze, N., Josset, D., and Gassó, S.: Spaceborne observations of the lidar ratio of marine aerosols, Atmos. Chem. Phys., 15, 3241–3255, https://doi.org/10.5194/acp-15-3241-2015, 2015.

Düsing, S., Wehner, B., Seifert, P., Ansmann, A., Baars, H., Ditas, F., Henning, S., Ma, N., Poulain, L., Siebert, H., Wiedensohler, A., and MacKe, A.: Helicopter-borne observations of the continental background aerosol in combination with remote sensing and ground-based measurements, Atmos. Chem. Phys., 18, 1263–1290, https://doi.org/10.5194/acp-18-1263-2018, 2018.

Düsing, S., Ansmann, A., Baars, H., Corbin, J. C., Denjean, C., Gysel-Beer, M., Müller, T., Poulain, L., Siebert, H., Spindler, G., Tuch, T., Wehner, B., and Wiedensohler, A.: Measurement report: Comparison of airborne, in situ measured, lidar-based, and modeled aerosol optical properties in the central European background -identifying sources of deviations, Atmos. Chem.

690 Phys., 21, 16745–16773, https://doi.org/10.5194/acp-21-16745-2021, 2021.

F. Cavalli, M. Viana, K. E. Yttri, J. Genberg, and J.-P. P.: Toward a standardised thermal-optical protocol for measuring atmospheric organic and elemental carbon: the EUSAAR protocol, https://doi.org/10.1080/00223348708572555, 2010.

Feingold, G., ~~L. A.~~ Remer, ~~L. A.,~~J. Ramaprasad, ~~J.,~~ and ~~Y. J.~~ Kaufman~~, Y. J.~~ (2001), Analysis of smoke impact on clouds in Brazilian biomass burning regions: An extension of Twomey's approach, J. Geophys. Res., 106(D19), 22907–22922,
695 ~~https://~~doi~~.org/~~:10.1029/2001JD000732.

Fernald, F. G.: Analysis of atmospheric lidar observations: some comments, Appl. Opt., 23, 652–653, https://doi.org/10.1364/AO.23.000652, 1984. https://doi.org/10.1364/AO.23.000652

Fernández, A. J., Apituley, A., Veselovskii, I., Suvorina, A., Henzing, J., Pujadas, M., and Artíñano, B.: Study of aerosol hygroscopic events over the Cabauw experimental site for atmospheric research (CESAR) using the multi-wavelength Raman
700 lidar Caeli, Atmos. Environ., 120, 484–498, https://doi.org/10.1016/j.atmosenv.2015.08.079, 2015.

Ferrero, L., Ritter, C., Cappelletti, D., Moroni, B., Močnik, G., Mazzola, M., Lupi, A., Becagli, S., Traversi, R., Cataldi, M., Neuber, R., Vitale, V., and Bolzacchini, E.: Aerosol optical properties in the Arctic: The role of aerosol chemistry and dust composition in a closure experiment between Lidar and tethered balloon vertical profiles, Sci. Total Environ., 686, 452–467, https://doi.org/10.1016/j.scitotenv.2019.05.399, 2019.

705 Floutsi, A. A., Baars, H., Engelmann, R., Althausen, D., Ansmann, A., Bohlmann, S., Heese, B., Hofer, J., Kanitz, T., Haarig, M., Ohneiser, K., Radenz, M., Seifert, P., Skupin, A., Yin, Z., Abdullaev, S. F., Komppula, M., Filioglou, M., Giannakaki, E., Stachlewska, I. S., Janicka, L., Bortoli, D., Marinou, E., Amiridis, V., Gialitaki, A., Mamouri, R. E., Barja, B., and Wandinger, U.: DeLiAn - a growing collection of depolarization ratio, lidar ratio and Ångström exponent for different aerosol types and mixtures from ground-based lidar observations, Atmos. Meas. Tech., 16, 2353–2379, https://doi.org/10.5194/amt-16-2353-
710 2023, 2023.

Fröhlich, R., Cubison, M. J., Slowik, J. G., Bukowiecki, N., Prévôt, A. S. H., Baltensperger, U., Schneider, J., Kimmel, J. R., Gonin, M., Rohner, U., Worsnop, D. R., and Jayne, J. T.: The ToF-ACSM: A portable aerosol chemical speciation monitor with TOFMS detection, Atmos. Meas. Tech., 6, 3225–3241, https://doi.org/10.5194/amt-6-3225-2013, 2013.

Geisinger, A., Behrendt, A., Wulfmeyer, V., Strohbach, J., Förstner, J., and Potthast, R.: Development and application of a
715 backscatter lidar forward operator for quantitative validation of aerosol dispersion models and future data assimilation, Atmos. Meas. Tech., 10, 4705–4726, https://doi.org/10.5194/amt-10-4705-2017, 2017.

~~Hans F. Graf~~~~,~~, H.-F.: The ~~Complex Interaction~~complex interaction of ~~Aerosols~~aerosols and ~~Clouds. Science303,~~clouds, Science (80-.)., 303, 1309~~-~~–1311~~(, 2004). https://doi.org/~~. DOI:10.1126/science.1094411~~.~~

Groß, S., Esselborn, M., Weinzierl, B., Wirth, M., Fix, A., and Petzold, A.: Aerosol classification by airborne high spectral
720 resolution lidar observations, Atmos. Chem. Phys., 13, 2487–2505, https://doi.org/10.5194/acp-13-2487-2013, 2013.

Haarig, M., Walser, A., Ansmann, A., Dollner, M., Althausen, D., Sauer, D., Farrell, D., and Weinzierl, B.: Profiles of cloud condensation nuclei, dust mass concentration, and ice-nucleating-particle-relevant aerosol properties in the Saharan Air Layer over Barbados from polarization lidar and airborne in situ measurements, Atmos. Chem. Phys., 19, 13773–13788, https://doi.org/10.5194/acp-19-13773-2019, 2019.

725 Heintzenberg, J. and Charlson, R. J.: Design and applications of the integrating nephelometer: A review, https://doi.org/10.1175/1520-0426(1996)013<0987:DAAOTI>2.0.CO;2, 1996.

Hervo, M., Poltera, Y., and Haefele, A.: An empirical method to correct for temperature-dependent variations in the overlap function of CHM15k ceilometers, 2947–2959, https://doi.org/10.5194/amt-9-2947-2016, 2016.

Illingworth, A. J., Barker, H. W., Beljaars, A., Ceccaldi, M., Chepfer, H., Clerbaux, N., Cole, J., Delanoë, J., Domenech, C.,
730 Donovan, D. P., Fukuda, S., Hirakata, M., Hogan, R. J., Huenerbein, A., Kollias, P., Kubota, T., Nakajima, T., Nakajima, T. Y., Nishizawa, T., Ohno, Y., Okamoto, H., Oki, R., Sato, K., Satoh, M., Shephard, M. W., Velázquez-Blázquez, A., Wandinger, U., Wehr, T., and Van Zadelhoff, G. J.: The earthcare satellite : The next step forward in global measurements of clouds, aerosols, precipitation, and radiation, Bull. Am. Meteorol. Soc., 96, 1311–1332, https://doi.org/10.1175/BAMS-D-12-00227.1, 2015.

735 ~~IPCC, A. R.: Climate change 2013: the physical science basis, Contrib. Work. Gr. I to fifth Assess. Rep. Intergov. panel Clim. Chang., 1535, 2013.~~

IPCC, 2013: Climate Change 2013: The Physical Science Basis. Contribution of Working Group I to the Fifth Assessment Report of the Intergovernmental Panel on Climate Change [Stocker, T.F., D. Qin, G.-K. Plattner, M. Tignor, S.K. Allen, J. Boschung, A. Nauels, Y. Xia, V. Bex and P.M. Midgley (eds.)]. Cambridge University Press, Cambridge, United Kingdom
740 and New York, NY, USA, 1535 pp. https://www.ipcc.ch/report/ar5/wg1/

Karanasiou, A., Panteliadis, P., Perez, N., Minguillón, M. C., Pandolfi, M., Titos, G., Viana, M., Moreno, T., Querol, X., and Alastuey, A.: Evaluation of the Semi-Continuous OCEC analyzer performance with the EUSAAR2 protocol, Sci. Total Environ., 747, https://doi.org/10.1016/j.scitotenv.2020.141266, 2020.

Kaufman, Y. J., Koren, I., Remer, L. A., Rosenfeld, D., and Rudich, Y.: The effect of smoke, dust, and pollution aerosol on
745 shallow cloud development over the Atlantic Ocean, Proc. Natl. Acad. Sci. U. S. A., 102, 11207–11212, https://doi.org/10.1073/pnas.0505191102, 2005.

~~Kim, S. W., Yoon, S. C., Kim, J., and Kim, S. Y.: Seasonal and monthly variations of columnar aerosol optical properties over east Asia determined from multi-year MODIS, LIDAR, and AERONET Sun/sky radiometer measurements, Atmos. Environ., 41, 1634-1651, https://doi.org/10.1016/j.atmosenv.2006.10.044, 2007.~~

750 Klett, J. D.: Stable analytical inversion solution for processing lidar returns, Appl. Opt., 20, 211–220, https://doi.org/10.1364/AO.20.000211, 1981.

Koren, I., Martins, J. V., Remer, L. A., and Afargan, H.: Smoke Invigoration Versus Inhibition of Clouds over the Amazon, Science (80-.)., 321, 946–949, https://doi.org/10.1126/science.1159185, 2008.

755 Liu, X., Henzing, B., Hensen, A., Dintherand, D. van, and Dusek, U.: Datasets for " Evaluation of the TOF-ACSM-CV for PM1.0 and PM2.5 measurements during the RITA-2021 field campaign," Zenodo, https://doi.org/10.5281/zenodo.7924288, 2023a.

Liu, X., Henzing, B., Hensen, A., Mulder, J., Yao, P., van Dinther, D., van Bronckhorst, J., Huang, R., and Dusek, U.: Measurement report: Evaluation of the TOF-ACSM-CV for PM1.0 and PM2.5 measurements during the RITA-2021 field campaign, EGUsphere [preprint],Atmos. Chem. Phys., 24, 3405–3420, https://doi.org/10.5194/egusphere 2023 967, 760 2023.acp-24-3405-2024, 2024.

Lohmann, U. and Feichter, J.: Global indirect aerosol effects: a review, Atmos. Chem. Phys., 5, 715–737, 2005. https://doi.org/10.5194/acp-5-715-2005, 2005.

Lopes, F. J. S., Landulfo, E., and Vaughan, M. A.: Evaluating CALIPSO's 532 nm lidar ratio selection algorithm using AERONET sun photometers in Brazil, Atmos. Meas. Tech., 6, 3281–3299, https://doi.org/10.5194/amt 6 3281 2013, 2013.

765 Lufft: User Manual Lufft CHM 15K Ceilometer, 2019.

Markowicz, K. M., Chilinski, M. T., Lisok, J., Zawadzka, O., Stachlewska, I. S., Janicka, L., Rozwadowska, A., Makuch, P., Pakszys, P., Zielinski, T., Petelski, T., Posyniak, M., Pietruczuk, A., Szkop, A., and Westphal, D. L.: Study of aerosol optical properties during long-range transport of biomass burning from Canada to Central Europe in July 2013, J. Aerosol Sci., 101, 156–173, https://doi.org/10.1016/j.jaerosci.2016.08.006, 2016. http://ferrarese.bo.isac.cnr.it/~elisabet/sites/default/files/2020-770 11/Manual_CHM15k_EN_R15_0.pdf

Mattis, I., Ansmann, A., Müller, D., Wandinger, U., and Althausen, D.: Multilayer aerosol observations with dual-wavelength Raman lidar in the framework of EARLINET, J. Geophys. Res. D Atmos., 109, https://doi.org/10.1029/2004JD004600, 2004.

Mattis, I., D'Amico, G., Baars, H., Amodeo, A., Madonna, F., and Iarlori, M.: EARLINET Single Calculus Chain – Technical – Part 2: Calculation of optical products, Atmos. Meas. Tech., 9, 3009–3029, https://doi.org/10.5194/amt 9 3009 2016, 2016.

775 Melfi, S. H.: Remote measurements of the atmosphere using Raman scattering., Appl. Opt., 11, 1605–1610, https://doi.org/10.1364/AO.11.001605, 1972.

Measures, R. M.: Laser remote sensing: Fundamentals and applications(Book), New York, Wiley-Interscience, 1984, 521 p, 1984.ISBN: 0471081930

Modini, R. L., Corbin, J. C., Brem, B. T., Irwin, M., Bertò, M., Pileci, R. E., Fetfatzis, P., Eleftheriadis, K., Henzing, B., 780 Moerman, M. M., Liu, F., Müller, T., and Gysel-Beer, M.: Detailed characterization of the CAPS single-scattering albedo monitor (CAPS PMssa) as a field-deployable instrument for measuring aerosol light absorption with the extinction-minus-scattering method, Atmos. Meas. Tech., 14, 819–851, https://doi.org/10.5194/amt-14-819-2021, 2021.

Moise, T., Flores, J. M., and Rudich, Y.: Optical Properties of Secondary Organic Aerosols and Their Changes by Chemical Processes, Chem. Rev., 115, 4400–4439, https://doi.org/10.1021/cr5005259, 2015.

785 Muller, T., Nowak, A., Wiedensohler, A., Sheridan, P., Laborde, M., Covert, D. S., Marinoni, A., Imre, K., Henzing, B., Roger, J. C., Dos Santos, S. M., Wilhelm, R., Wang, Y. Q., and De Leeuw, G.: Angular illumination and truncation of three different integrating nephelometers: Implications for empirical, size-based corrections, Aerosol Sci. Technol., 43, 581–586, https://doi.org/10.1080/02786820902798484, 2009.

Noh, Y. M., Kim, Y. J., and Müller, D.: Seasonal characteristics of lidar ratios measured with a Raman lidar at Gwangju, Korea 790 in spring and autumn, Atmos. Environ., 42, 2208–2224, https://doi.org/10.1016/j.atmosenv.2007.11.045, 2008.

Peters, T. M. and Leith, D.: Concentration measurement and counting efficiency of the aerodynamic particle sizer 3321, J. Aerosol Sci., 34, 627–634, https://doi.org/10.1016/S0021-8502(03)00030-2, 2003.

Petters, M. D. and Kreidenweis, S. M.: A single parameter representation of hygroscopic growth and cloud condensation nucleus activity-Part 3: Including surfactant partitioning, Atmos. Chem. Phys., 13, 1081–1091, https://doi.org/10.5194/acp-795 13-1081-2013, 2007.

Petzold, A. and Schönlinner, M.: Multi-angle absorption photometry—a new method for the measurement of aerosol light absorption and atmospheric black carbon, J. Aerosol Sci., 35, 421–441, https://doi.org/https://doi.org/10.1016/j.jaerosci.2003.09.005, 2004.

Petzold, A., Schloesser, H., Sheridan, P. J., Arnott, W. P., Ogren, J. A., and Virkkula, A.: Evaluation of multiangle absorption 800 photometry for measuring aerosol light absorption, Aerosol Sci. Technol., 39, 40–51, https://doi.org/10.1080/027868290901945, 2005.

Potenza, M. A. C., Albani, S., Delmonte, B., Villa, S., Sanvito, T., Paroli, B., Pullia, A., Baccolo, G., Mahowald, N., and Maggi, V.: Shape and size constraints on dust optical properties from the Dome C ice core, Antarctica, Sci. Rep., 6, 1–9, https://doi.org/10.1038/srep28162, 2016.

805 Rolph, G., Stein, A., and Stunder, B.: Real-time Environmental Applications and Display sYstem: READY, Environ. Model. Softw., 95, 210–228, https://doi.org/10.1016/j.envsoft.2017.06.025, 2017.

Rosati, B., Herrmann, E., Bucci, S., Fierli, F., Cairo, F., Gysel, M., Tillmann, R., Größ, J., Paolo Gobbi, G., Di Liberto, L., Di Donfrancesco, G., Wiedensohler, A., Weingartner, E., Virtanen, A., F Mentel, T., and Baltensperger, U.: Studying the vertical aerosol extinction coefficient by comparing in situ airborne data and elastic backscatter lidar, Atmos. Chem. Phys., 16, 4539–810 4554, https://doi.org/10.5194/acp-16-4539-2016, 2016.

Rosenfeld, D., Sherwood, S., Wood, R., and Donner, L.: Climate effects of aerosol-cloud interactions, Science, (80-.)., 343, 379–380, 2014. https://doi.org/10.1126/science.1247490.

Salemink, H. W. M., Schotanus, P., and Bergwerff, J. B.: Quantitative lidar at 532 nm for vertical extinction profiles and the

effect of relative humidity, Appl. Phys. B Photophysics Laser Chem., 34, 187–189, https://doi.org/10.1007/BF00697633, 1984.

815   Schaap, M., Weijers, E. ., Mooibroek, D., Nguyen, L., and Hoogerbrugge, R.: Composition and origin of particulate matter in the Netherlands, RIVM Rapp., 69, 2010. https://www.pbl.nl/sites/default/files/downloads/500099007.pdf

Shin, S. K., Tesche, M., Kim, K., Kezoudi, M., Tatarov, B., Müller, D., and Noh, Y.: On the spectral depolarisation and lidar ratio of mineral dust provided in the AERONET version 3 inversion product, Atmos. Chem. Phys., 18, 12735–12746, https://doi.org/10.5194/acp-18-12735-2018, 2018.

820   Sicard, M., Rocadenbosch, F., Reba, M. N. M., ComerÓn, A., Tomás, S., García-Vízcaino, D., Batet, O., Barrios, R., Kumar, D., and Baldasano, J. M.: Seasonal variability of aerosol optical properties observed by means of a Raman lidar at an EARLINET site over Northeastern Spain, Atmos. Chem. Phys., 11, 175–190, https://doi.org/10.5194/acp-11-175-2011, 2011.

Stein, A. F., Draxler, R. R., Rolph, G. D., Stunder, B. J. B., Cohen, M. D., and Ngan, F.: Noaa's hysplit atmospheric transport and dispersion modeling system, Bull. Am. Meteorol. Soc., 96, 2059–2077, https://doi.org/10.1175/BAMS-D-14-00110.1,
825   2015.

Sumlin, B. J., Heinson, W. R., and Chakrabarty, R. K.: Retrieving the aerosol complex refractive index using PyMieScatt: A Mie computational package with visualization capabilities, J. Quant. Spectrosc. Radiat. Transf., 205, 127–134, https://doi.org/10.1016/j.jqsrt.2017.10.012, 2018.

Twomey, S.: The Influence of Pollution on the Shortwave Albedo of Clouds, J. Atmos. Sci., 34, 1149–1152,
830   https://doi.org/https://doi.org/10.1175/1520-0469(1977)034<1149:TIOPOT>2.0.CO;2, 1977.

Wandinger, U.: Introduction to lidar, in: Lidar: range-resolved optical remote sensing of the atmosphere, Springer, 1–18, 2005. https://doi.org/10.1007/b106786

Wandinger, U. and Ansmann, A.: Experimental determination of the lidar overlap profile with Raman lidar, Appl. Opt., 41, 511, https://doi.org/10.1364/ao.41.000511, 2002.

835   Weitkamp, C.: Range-resolved optical remote sensing of the Atmosphere, Springer-Verlag New York, 102, 241–303, 2005.ISBN: 978-0-387-40075-4

Whiteman, D. N., Melfi, S. H., and Ferrare, R. A.: Raman lidar system for the measurement of water vapor and aerosols in the Earth's atmosphere, Appl. Opt., 31, 3068–3082, https://doi.org/10.1364/AO.31.003068, 1992.

Wiedensohler, A., Birmili, W., Nowak, A., Sonntag, A., Weinhold, K., Merkel, M., Wehner, B., Tuch, T., Pfeifer, S., Fiebig,
840   M., Fjäraa, A. M., Asmi, E., Sellegri, K., Depuy, R., Venzac, H., Villani, P., Laj, P., Aalto, P., Ogren, J. A., Swietlicki, E., Williams, P., Roldin, P., Quincey, P., Hüglin, C., Fierz-Schmidhauser, R., Gysel, M., Weingartner, E., Riccobono, F., Santos, S., Grüning, C., Faloon, K., Beddows, D., Harrison, R., Monahan, C., Jennings, S. G., O'Dowd, C. D., Marinoni, A., Horn, H. G., Keck, L., Jiang, J., Scheckman, J., McMurry, P. H., Deng, Z., Zhao, C. S., Moerman, M., Henzing, B., De Leeuw, G., Löschau, G., and Bastian, S.: Mobility particle size spectrometers: Harmonization of technical standards and data structure to

845 facilitate high quality long-term observations of atmospheric particle number size distributions, Atmos. Meas. Tech., 5, 657–685, https://doi.org/10.5194/amt-5-657-2012, 2012.

Wiegner, M. and Geiß, A.: Aerosol profiling with the Jenoptik ceilometer CHM15kx, Atmos. Meas. Tech., 5, 1953–1964, https://doi.org/10.5194/amt-5-1953-2012, 2012.

Zhang, Z., Shen, Y., Li, Y., Zhu, B., and Yu, X.: Analysis of extinction properties as a function of relative humidity using a κ-
850 EC-Mie model in Nanjing, Atmos. Chem. Phys., 17, 4147–4157, https://doi.org/10.5194/acp-17-4147-2017, 2017.

Zieger, P., Väisänen, O., Corbin, J. C., Partridge, D. G., Bastelberger, S., Mousavi-Fard, M., Rosati, B., Gysel, M., Krieger, U. K., Leck, C., Nenes, A., Riipinen, I., Virtanen, A., and Salter, M. E.: Revising the hygroscopicity of inorganic sea salt particles, Nat. Commun., 8, https://doi.org/10.1038/ncomms15883, 2017.

Zou, J., Yang, S., Hu, B., Liu, Z., Gao, W., Xu, H., Du, C., Wei, J., Ma, Y., Ji, D., and Wang, Y.: A closure study of aerosol
855 optical properties as a function of RH using a K-AMS-BC-Mie model in Beijing, China, Atmos. Environ., 197, 1–13, https://doi.org/10.1016/j.atmosenv.2018.10.015, 2019.